

國立交通大學

材料科學與工程所

博士論文

低溫共燒陶瓷的介電性質量測與燒結匹配性研究

研究生：饒瑞榆

指導教授：林鵬 教授

中華民國九十六年七月

低溫共燒陶瓷的介電性質量測與燒結匹配性研究
The study dielectric measurement and sintering match of LTCC

研究生：饒瑞榆

Student : Jui-Yu, Jao

指導教授：林鵬

Advisor : Pang Lin



Submitted to Institute of Material Science and Engineering

National Chiao Tung University

in partial Fulfillment of the Requirements

for the Degree of

PhD

in

Material Science and Engineering

July 2007

Hsinchu, TaiwanChina, Republic of China

中華民國九十六年七月

低溫共燒陶瓷的介電性質量測與燒結匹配性研究

學生：饒瑞榆

指導教授：林鵬

國立交通大學材料科學與工程研究所 博士班

中文摘要

低溫共燒陶瓷(Low temperature co-fired ceramic, LTCC) 的燒結是決定整個元件特性的關鍵。燒結後的介電常數的評估，及材料配方調整以得到較小的燒結所造成的變異，及獲得較好的燒結匹配，是這篇論文研究的重點。論文包含三個部分：第一部份是提出一個計算在低溫共燒陶瓷元件的介電常數(ϵ)方法，此計算方法是利用帶通濾波器的第二諧振頻率 (Second Harmonic Frequency, SHF) 與介電常數的關連性。 ϵ -SHF的關係式可透過模擬來得到，加上量測到 BPF 的 SHF，就可以計算出介電常數。這些計算出來的介電常數，與傳統以 pellet 量測到的介電常數非常相近。

第二部分是提出兩個共燒材料，藉由不同軟化點(onset shrinkage temperature, OST) 及結晶溫度 (crystallization temperature, CRT)，在燒結時互相抑制對方在 X/Y 方向的收縮，以達

到 X/Y 方向收縮只有0.2% (最高燒結溫度在 880°C，降低了燒結所造成的變異。OST溫度 (802 °C到606 °C)是藉由不同 Na₂O (0-1.0wt%)比例添加在 CaO-SiO₂ 玻璃所控制，而燒結條件也扮演很重要的角色。這兩個材料經由不同 Na₂O 比例及燒結條件，會造成不同的燒結收縮率，但所量測到的介電常數卻差異不大，都是在 6 附近。

第三部份探討 LTCC 與 Ni-Cu-Zn ferrite 共燒情形。將Ni-Cu-Zn ferrite 埋入 B₂O₃-SiO₂ 中，在塗上銀電極作成電感。發現添加 35wt% Al₂O₃在B₂O₃-SiO₂中，與加有 2wt% Bi₂O₃的 Ni-Cu-Zn ferrite 可以克服燒結不匹配造成的翹曲及裂痕，並且將Ni-Cu-Zn ferrite埋入B₂O₃-SiO₂中，可以提高電感的感值與品質因子。



The study dielectric measurement and sintering match of LTCC

Student : Jui-Yu, Jao

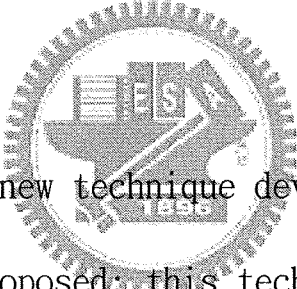
Advisors : Dr. Pang Lin

Institute of Material Science and Engineering
National Chiao Tung University

ABSTRACT

The sintering behavior of low temperature co-fired ceramic (LTCC) is a key to decide the device characteristics. The way to evaluate the electronic characteristics after sintering, and what kind of material composition has better sintering match are the major topics in this paper. This thesis is composed of three parts. In the first one, a method of estimating the dielectric constant (ϵ) of dielectric layers in LTCC devices was developed. A band-pass filter (BPF) circuit was designed such that its second harmonic frequency (SHF) strongly depended on the ϵ of the relevant capacitor built in the BPF. The ϵ - SHF correlation was

established by model simulation. The design of the BPF was realized with various dielectric layers, and the measured SHF was used to determine the ϵ values of the capacitors from the ϵ - SHF relationship. These ϵ values were found to be consistent with those of the sintered pellets, prepared with the same dielectrics and process as BPFs. The ϵ values of the dielectric layers in other LTCC devices were estimated by this method, in which the BPFs made of the same dielectric layers were fired as dummy samples along with the devices.



The second part, a new technique developed for the low shrinkage of LTCC is proposed; this technique is based on a self-constraining mechanism, which relies on composite green tapes formed by two laminated glass layers, each of which has a distinct softening point (onset shrinkage temperature, OST) and a crystallization temperature (CRT). Each layer works as a constraining layer for the other layer in a distinct temperature range to prevent excessive linear shrinkage along the layer plane. The OSTs ranging from 802 to 606°C are adjusted by controlling the

amount of Na_2O (0~1.0 wt%) added to the CaO-SiO_2 glass. The OST and CRT of the two glass layers as well as the heating profile have strong effects on shrinkage ratio, the lowest of which is found to be only 0.2% after sintering up to 880°C . The measured dielectric constant of the sintered samples is approximately 6.0 within a narrow variation range even when the samples have a wide range of shrinkage ratios.

The last one, inductors using a new LTCC design, that Ni-Cu-Zn ferrite was buried in $\text{B}_2\text{O}_3\text{-SiO}_2$ glass within the core of spiral silver coil, were fabricated. The inductance and quality factor of inductor with embedded ferrite are larger than that of pure $\text{B}_2\text{O}_3\text{-SiO}_2$ glass. Ni-Cu-Zn ferrite was incompatible with the $\text{B}_2\text{O}_3\text{-SiO}_2$ glass during the co-firing process due to sintering shrinkage mismatch. The incompatibility was resolved when 35wt% Al_2O_3 was added into $\text{B}_2\text{O}_3\text{-SiO}_2$ glass, which produces glass-ceramic, and 2wt% of Bi_2O_3 was fluxed into the Ni-Cu-Zn ferrite as sintering aid. Addition of 2wt% of Bi_2O_3 not only enhances the densification, but also increases the permeability of Ni-Cu-Zn ferrite.

誌謝

感謝指導教授林鵬老師八年來的耐心教導，讓我在專業知識上獲益良多，並使本論文得以完成，在此致上最誠摯的敬意與感謝。交通大學陳三元老師，曾俊元教授及台北科技大學資材所所長王錫福教授，中正大學湯敬文教授，成功大學向性一教授，高雄醫學大學石啟仁教授於口試時對本論文的建議及指正，使得本論文更臻完美，在此亦表由衷謝意。特別感謝王錫福教授於論文撰寫上的指導與修正，讓我順利完成博士學位。此外，感謝實驗室學弟盧俊安，劉元文對課業及研究事務上的協助及遠東大學蕭富昌教授的大力幫忙。感謝成功大學顏富士教授及黃啟原教授的支持鼓勵。最後，謹將本文獻給親愛的家人，老公及心肝寶貝逸陽跟語晴。

This work was supported by the National Science Council of the Republic of China under Contract No. NSC 90-2216-E-009-039.

Compared Table

1	LTCC	Low Temperature Co-fired Ceramic
2	ϵ	Dielectric constant
3	BPF	Band pass filter
4	SHF	Second harmonic frequency
5	OST	Onset shrinkage temperature
6	CRT	Crystallization temperature
7	RF	Radio frequency
8	WLAN	Wireless local area network
9	SL	Step impedance transmission line
10	CT	Composite tape
11	C_{SL}	Equivalent capacitor
12	L_{SL}	Equivalent inductor
13	w	Inductor line width
14	Δ	Thickness
15	μ_i	Permeability

Contents

Abstract(in Chinese)	i
Abstract(in English)	iii
Acknowledgment (in Chinese)	vi
Compared Table.....	vii
Contents	viii
Figure Caption.....	viii
Table Caption.....	xii
Chapter 1 Overview.....	1
Chapter 2 Method of estimating dielectric properties of dielectric layers	9
2-1 Experimental procedure.....	9
2-2 Results and discussion.....	13
2-3 Conclusions.....	17
Chapter 3 Self-constraining method for low shrinkage.....	24
3-1 Experimental procedure.....	24
3-2 Results and discussion.....	27
3-3 Conclusions.....	31
Chapter 4 Characterization of inductor with Ni-Cu-Zn ferrite embedded in $B_2O_3-SiO_2$ glass.....	42
4-1 Experimental procedure.....	42
4-2 Results and discussion.....	45
4-3 Conclusions.....	51
Chapter 5 Summary.....	62
Reference	65
Resume (in Chinese)	70
Publication list.....	72

Figure Caption

- Fig.1. Equivalent circuit of multilayer BPF, the quarter-wavelength SL is represented by L_{SL} and C_{SL}18
- Fig.2. Typical simulation results for BPF frequency response, obtained using scheme in Fig. 1, where ϵ of SL capacitor was set to be 7.7 and capacitor thickness, 40 and 43 μm . SHF is indicated by an arrow.19
- Fig.3. SHFs obtained by simulation with series of preset dielectric constants ranging from 7.0 to 8.0, for various SL capacitor thicknesses from 40 to 43 μm20
- Fig.4. Typical frequency response spectrum measured from fabricated BPFs.21
- Fig.5. SEM images of fractured surfaces of pellets made from $\text{BaAl}_2\text{Si}_2\text{O}_8$ glass powders with particle sizes of (a) 2.3, (b) 2.2, (c) 1.6, (d) 1.4, and (e) 1.1 μm22
- Fig.6. Measured linear shrinkage ratio along plane of individual. tape A and B series heated in thermal mechanical analyzer at heating rate of $3^\circ\text{C}/\text{min}$, showing onset shrinkage temperature (OST) of each glass.32
- Fig.7. Differential thermal analysis of glasses A and B series carried out at $10^\circ\text{C}/\text{min}$, showing temperature of crystallization of each glass.33

Fig.8. Typical x-ray diffraction results of the crystallized glass A and B series, indicating crystalline phase $\text{Ca}_3\text{Si}_3\text{O}_9$	34
Fig.9. Two sets of thermal profiles I (9a) and II (9b) adopted in the TMA for the test of the shrinkage behavior of samples A/B1, A/B2, A/B3 and A. They have the same heating rate of $3^\circ\text{C}/\text{min}$ but I has an extra constant-temperature duration at 650°C	35
Fig.10. Shrinkage curves of samples A/B2 and A/B3 heated using profile I, showing total shrinkage of A/B2 of only 0.2%.	36
Fig.11. Microstructure observed by SEM on A/B2 sample surface with thermal etching treatment, showing crystallized grains of $1.2\ \mu\text{m}$ average size.	37
Fig.12. Fractured cross section of sample A/B2 and associated EDS image, revealing crystallized grains in internal structure and sodium element (gray spots) distribution in tape B2.	38
Fig.13. Design of chip inductors with six-layer coil.....	52
Fig.14. Sintering profile for the inductor.....	53
Fig.15. Sintering shrinkages of Ni-Cu-Zn ferrites with various amounts of Bi_2O_3 additions.....	54

Fig.16. SEM micrographs of Ni-Cu-Zn ferrites sintered with various amounts of Bi ₂ O ₃ additions.	55
Fig.17. Permeability versus frequency curves for Ni-Cu-Zn Ferrite with various amounts of Bi ₂ O ₃ addition and sintered at 860 °C.	56
Fig.18. Sintering shrinkages of B ₂ O ₃ -SiO ₂ glass with various amounts of Al ₂ O ₃ addition.	57
Fig.19. SEM micrographs of 2 wt% Bi ₂ O ₃ added Ni-Cu-Zn ferrite co-fired with B ₂ O ₃ -SiO ₂ glass with various amounts of Al ₂ O ₃ addition at 860□°C.	58
Fig.20. Sintering compatibility study of the Ni-Cu-Zn ferrite and B ₂ O ₃ -SiO ₂ glass.	59
Fig.21. Frequency dependences of the inductance and quality Factor for the inductor with embedded spiral coils.	60

Table Caption

Table I. (a)-(e). Each subtable shows the particle size of the glass powder, from which the BPFs and pellets were fabricated; it also shows the thickness Δ of the SL capacitors, the SHFs measured from the BPFs, the values evaluated from the SHF - ϵ relationship, the ϵ_p values measured from the pellets, and pore sizes and porosities measured from the fractured surfaces of the pellets. The accuracy range for SHF is about $\pm 0.17\%$, that for ϵ is about ± 0.025 and that for ϵ_p is about ± 0.0423

Table II. Onset shrinkage temperatures and crystallization temperatures of CaO-SiO₂ glass layers with different Na₂O contents.39

Table III. Shrinkage ratios of composite tapes made of glass layers A and B series sintered in profiles I and II.40

Table IV. Dielectric constants of composite tapes made of glass. . layers A and B series sintered in profiles I and II.41

Table V. Characteristics of the Ni-Cu-Zn ferrite with various. . amounts of Bi₂O₃ additions.61

Chapter 1 Overview

The sintering behavior of low temperature co-fired ceramic (LTCC) is a key to decide the device characteristics. The way to evaluate the electronic characteristics after sintering, and what kind of material composition has better sintering match are the major topics in this paper.

A band-pass filter (BPF) is one of the key components in a radio frequency (RF) front end for wireless local area network (WLAN) application.¹⁻⁸⁾ It does not only select pass-band frequency, but also reject an image signal and suppress second harmonic intensity.⁹⁾ For a BPF with preset dimensions and structure, second harmonic frequency (SHF) is mainly determined by the dielectric constant (ϵ) and thickness of the step-impedance-transmission-line (SL) capacitor built in the BPF.¹⁰⁾ If the correlation between SHF and ϵ (with SL capacitor thickness as a fixed parameter) were established by model simulation, it would be useful in evaluating the dielectric constant of the capacitor in a real BPF from the

measured SHF by referring to the above-mentioned simulated SHF - ϵ relationship. In this study, a BPF system was deliberately designed to have a highly sensitive SHF response to the ϵ variation of an SL capacitor, such that a highly accurate ϵ could be determined. On the other hand, real BPFs were fabricated by LTCC method using the three-dimensional structure transformed from this circuit scheme. The ϵ values of SL capacitors in real BPFs were evaluated by this method and compared with those of the sintered pellets, prepared with the same dielectrics and thermal processing as the BPFs. The high degree of consistency found between them supported the proposed method.

LTCC materials tend to shrink during sintering. This shrinkage often causes defects inside LTCC devices.^{11,12)} Some manufacturers have developed low-shrinkage LTCC processes, in which shrinkage is allowed only in the z-direction perpendicular to the lamination plane of the devices.¹³⁻¹⁷⁾ In such processes, alumina green tapes or porous alumina plates are adopted as constraining layers. They were put on the top and bottom of LTCC

green tapes and laminated together to reduce the shrinkage in the x- and y-directions in the subsequent sintering. The constraining layers made of refractory alumina are not sintered at the sintering temperature of the LTCC. Therefore, no shrinkage occurs along the x- and y-directions of alumina layers, and the constraining force applied on the neighboring layers leads to a very low shrinkage of LTCC layers in their plane.

However, some drawbacks of the above techniques have been reported: 1). Among laminated green layers, those closer to the external constraining layer showed less shrinkage along the x/y-direction than those the far away.¹⁸⁾ Hence, the x/y shrinkage amount is not uniform along the z-axis that may cause x/y-plane stress and microcracks inside the devices there by reducing their reliability. 2). Predesigned cavities normally could be punched on green tapes, so that the space of the cavities on LTCC devices after the sintering could be reserved for embedding IC chips. However, with external constrain, the process becomes impractical because of the local deformation of the cavities due to the

non-uniform shrinkage distribution along the z-direction as mentioned in 1). Well-shaped cavities can only be formed by laser machining on the surface of the sintered device. 3) Conductor wires, which were printed previously on the device surface and cofired with a green LTCC module, might bond to the external constraining layer and peel off the device surface when the constraining layers are removed by mechanical force, such as sand blasting.

In this study, a new technique for low-shrinkage LTCCs based on a self-constraining mechanism was developed. In this technique, the green tape adopted is a composite tape (CT) made of two laminated glass layers, each of which has a distinct onset shrinkage temperature (OST, the temperature at which glass tape sufficiently softens and starts to sinter, and shrink in the absence of constraint). The glass layer with the higher OST works as the constraining layer when the heating temperature reaches the lower OST of the other layer. The latter would start to sinter without shrinking. Assuming that glass could crystallize later

at a temperature below the higher OST, then the many crystallites that nucleated and grew in the layer would constitute a solid frame resisting shrinkage by itself. The layer with the crystallites, in turn, can work as the constraining layer when the neighboring glass layer starts to sinter at the higher OST. In practice, several alternate high- and low-OST layers would be laminated together (equivalent to several CTs laminated) for use in the devices. This arrangement would result in constraining force on both sides of each glass layer. The above self-constraining mechanism could prevent these drawbacks caused by the external constraining layers. In addition, this new technique allows more flexibility in LTCC module design at a lower processing cost.

In current research, glass with a higher OST consists mainly of CaO-SiO_2 glass. The OST of the glass can be lowered progressively by increasing the Na_2O content in the $\text{Na}_2\text{O-CaO-SiO}_2$ glass. To achieve low-shrinkage CT, glass tape with a suitable Na_2O content and an appropriate lower OST was selected to match that with the higher OST. The resulting shrinkage ratio along the

x-and y-directions of the CT can be reduced to 0.2%.

In addition to the conventional printed circuit board technology, LTCC technology is one of the new technologies to manufacture integrated multifunctional electronic chips. It can be utilized for the integration of passive components into a monolithic, high reliable and robust LTCC module. The module consists of several layers of substrate material with buried components such as capacitors, inductors, resistors, resonators, and filters. They are interconnected with 3-D strip-line circuitry. Utilization of low dielectric constant (ϵ) LTCC substrate materials and the associated high conductivity metallizations, such as Au and Ag, was found to have potential applications in the area of wireless communication.

Permeability of LTCC glass substrate is near unity, so it is difficult to make large value of inductors by printing spiral pattern of metals on the substrate. Inserting the layer of Ni-Cu-Zn ferrite into LTCC layers can increase permeability (μ_i)

and the inductance of the devices. Most Ni-Cu-Zn ferrites are incompatible with LTCC substrates during co-fired process. Sintering mismatch between these two materials leads to cambering or warping in the multilayer structure. To obtain a distortion-free LTCC multilayer substrate with buried ferrite, the sintering behaviors of these two dissimilar materials must be controlled and modified. Typical Ni-Cu-Zn ferrite with a regular particle size have sintering temperatures above 1100 °C. Reducing the sintering temperature of ferrite is inevitable in order for cofiring with LTCC substrate, since most substrates were fired at 850 to 900°C. It is reported in the literature that V_2O_5 , Na_2O , PbO , Bi_2O_3 , $3NiO \cdot V_2O_5$, $PbO \cdot SiO_2$ and Bi_2O_3 were effective sintering additives to promote the densification of Ni-Cu-Zn ferrites at a lower temperature¹⁹⁻²⁶⁾. $PbO \cdot SiO_2$ glass was found to significantly reduce the sintering temperature of ferrite and resulted in ceramics with a small and uniform grain size, and possessed higher resistivity, higher μ_i and higher Q , based on the study of Wang and his co-workers^{20, 21)}. However, the addition

of Bi_2O_3 considerably deteriorated the quality factor of Ni-Cu-Zn ferrites, though benefited the densification and permeability.

Though Chen et al. have successfully embedded a ferrite inductor layer into a LTCC module²⁷⁾, only a few literatures have been reported regarding the co-firing of a ferrite and LTCC substrate. In this study, inductor with a new design, in which Ni-Cu-Zn ferrite was buried in B_2O_3 - SiO_2 glass within the spiral silver coil, was fabricated. In order to eliminate the shrinkage mismatch, formulation of ferrite was tailored to control the onset densification temperature and the sintering shrinkage profile of Ni-Cu-Zn ferrite. Bi_2O_3 was chosen as the flux to reduce the sintering temperature of Ni-Cu-Zn ferrite, and, Al_2O_3 was added to retard the sintering shrinkage rate of B_2O_3 - SiO_2 glass through forming a glass-ceramic. The densification, micro-structural evolution and magnetic properties of the individual ceramics as well as the LTCC inductor were characterized and discussed.

Chapter 2 Method of estimating dielectric properties of dielectric layers

2-1 Experimental procedure

Figure 1 shows the equivalent circuit of a multilayer BPF. The quarter-wavelength SL (with an equivalent inductor and capacitor respectively denoted by L_{SL} and C_{SL}) suppresses second harmonic intensity. The circuit was designed in such a manner that SHF was very sensitive to the dielectric properties of the SL capacitor. The capacitances of C_{10} , C_{20} , C_{12} , C_{1L} , C_{2L} , and C_{SL} are 3.64, 0.5, 1.54, 7.6, 2.86, and 2.45 pF, respectively. The inductance of L_{SL} is 0.43 nH. SL_1 and SL_2 have dimensions of $4.77 \times 0.20 \text{ mm}^2$ and $6.73 \times 0.20 \text{ mm}^2$, respectively. On the basis of the circuit, the BPF frequency response was simulated using the SONNET V10.52 program (Sonnet Software), and the associated SHF was identified.

In addition to the dielectric constant ϵ and thickness Δ of the SL capacitor, other factors affecting SHF are printing pattern characteristics, such as the inductance line width w , the

variation of which is determined by fabrication techniques. Hence, a simulation was carried out to establish the SHF - ϵ relationship by varying, ϵ (from 7.0 to 8.0) and Δ (from 40 to 43 μm) with a fixed line width ($w = 150 \mu\text{m}$). The effect of changing w on SHF was also investigated at $\Delta = 40$ and $\epsilon = 7.7$ by simulation.

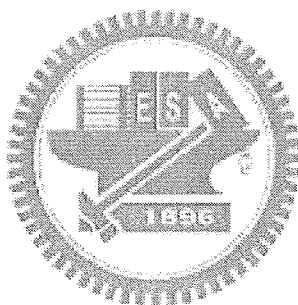
Low-temperature-cofirable glass powder (CT700, Heraeus) with the nominal composition $\text{BaAl}_2\text{Si}_2\text{O}_8$ was used to fabricate the BPF. The glass powder was ball-milled for 0, 6, 12, 24, and 48 h, and dried in a box oven. The average particle sizes of the milled powders estimated by scanning electron microscopy (SEM; Hitachi S-4700) were 3.8, 2.7, 2.2, 1.8, and 1.3 μm . The glass powders of different particle sizes were used to produce SL capacitors with different ϵ values. Slurry was prepared by mixing each type of powder with an organic vehicle containing a binder, a plasticizer and solvents. The slurry was then cast on a Mylar carrier to form green tapes, on which via-holes were punched and filled with Ag paste (TC 7301, Heraeus). Ag paste (TC 2304, Heraeus) was also deposited on the greens tape by screen printing to form

conductor lines. The printed tapes were laminated at a pressure of 20 MPa at 70 °C for 10 min to form a BPF structure, using the three-dimensional structure transformed from the circuit scheme in Fig. 1. The laminated tapes were singularized and terminated. The singularized green BPFs were heated at a rate of 3 °C /min from room temperature to 400 °C in air and then held for 2 h to remove the organic binder completely. The same heating rate was used up to 850 °C, where the BPF samples were held for 30 min before furnace cooling. The measured thicknesses of the fired tapes ranged from 40 to 43 μm .

To prepare pellets, the same series of glass powders used for the BPFs were mixed with 3 wt% ethylene glycol in acetone. After drying, the powders were uniaxially pressed at a pressure of 100 MPa to form pellets of 2 cm diameter and 0.8 cm height. These pellets were then fired using the same sintering profile as that of BPF.

The frequency response result of the sintered BPFs was measured using an HPE5071A meter to be from 1.5 to 5.5 GHz, from

SHF was identified. The ϵ (at 4.8GHz) of the fired pellets was measured with HP8719D and a cavity device (Resin-Model 200 Circular cavity, Domaskos) in transverse magnetic (TM) mode. A standard Al_2O_3 pellet was used as a reference sample for calibration. Repeated measurements on the same pellet gave ϵ values within a ± 0.6 % fluctuation. The microstructure of the pellets was observed by SEM.



2-2 Results and discussion

The typical simulation results for the BPF frequency response obtained using the scheme in Fig. 1 are shown in Fig. 2, where the ϵ of the SL capacitor was set to be 7.7 and the capacitor thickness Δ was set to be 40 and 43 μm . The assigned thickness range corresponds to the thickness tolerance of the fabricated SL capacitors. The variation in Δ , $\sim 3 \mu\text{m}$ (7.5% in ratio), led to a small change in SHF, $\sim 40 \text{ MHz}$ (0.8%), as indicated by an arrow in Fig. 2. The SHFs obtained by simulation with a series of preset dielectric constants ranging from 7.0 to 8.0 are shown in Fig. 3, for various Δ values from 40 to 43 μm and a line width of 150 μm . This figure shows that the small ϵ of the SL capacitor results in the high SHF of the BPF in an approximately linear manner, consistent with the study of Makimoto and Yamashita.²⁰⁾ A highly sensitive response of the SHF to the variation in ϵ is revealed in the plot, where the change in ϵ from 7.0 to 8.0 ($\sim 14\%$ in ratio) caused a shift in SHF from 5 to 4.7 GHz ($\sim 6\%$).

The simulation also showed that if the inductance line width

w deviates from the preset standard width of $150\ \mu\text{m}$ by $\pm 2\ \mu\text{m}$, SHF will change from $4.780\ \text{GHz}$ by $\pm 0.06\%$ (with the preset dielectric thickness $\Delta = 40\ \mu\text{m}$ and $\epsilon = 7.7$). SHF linearly changes with the width deviation. To reduce interference to SHF from the line width variation, only the fabricated BPFs with printing pattern widths lying within the limit of $150 \pm 2\ \mu\text{m}$ were evaluated in this study. Line width was measured on BPF cross sections by SEM using a coordinate measuring machine (VMR-10080, Nikon).

On the basis of the simulation results shown in Fig. 3, the ϵ -SHF relationship reveals a slope of $3.08/\text{GHz}$. Therefore, the error of SHF ($\pm 0.06\%$ or $\pm 0.0023\ \text{GHz}$) due to the variation in printing pattern width leads to an ϵ error of ± 0.009 .

The typical frequency response spectrum measured from the fabricated BPFs is presented in Fig. 4. The SHFs obtained from the real BPFs are listed in Table I, where each subtable includes the data derived from the samples made from the $\text{BaAl}_2\text{Si}_2\text{O}_8$ glass powders of the same particle size. SL capacitor thickness was evaluated by SEM on the cross section of each BPF sample. For each

particle size, 10 - 15 BPF samples were tested and their Δ values were found to fall within the range of 40 - 43 μm and classified at 1 μm intervals. The average SHF obtained from the samples at each interval was well differentiated from that of the neighboring interval. For each BPF sample, the frequency response spectrum was repeatedly measured 32 times, and most SHFs were found to vary within an error of $\pm 0.11\%$. In combination with the SHF error ($\pm 0.06\%$) from the pattern line width variation, the resultant error is about $\pm 0.17\%$. The corresponding ϵ error is ± 0.025 based on the ϵ -SHF relationship. It is noted that the ϵ error obtained by the SHF method is equivalent to $\sim \pm 0.33\%$ (consider $\epsilon \sim 7.3$) and less than that of pellets ($\sim \pm 0.6\%$ obtained by the cavity method). Using the measured SHF and Δ , the ϵ values of the real SL capacitors were determined by referring to the simulated ϵ -SHF plot in Fig. 3 as a reference curve. These SL capacitors made from the glass powders of the same particle size have, irrespective of their thickness, similar ϵ values, as observed in each subtable of Table I.

To verify the validity of the SHF method for obtaining ϵ , the ϵ values of the pellets, made from the same glass powders and treated by the same thermal process as the BPFs are listed in Table I for comparison. Each listed value is the average of more than ten times of measurements of the same pellet. The consistency between the values (see Table I) confirms the feasibility of this method based on the ϵ - SHF reference curve.

The ϵ values of the SL capacitors and pellets increased with the averaged particle size of the glass powders from which they were prepared. This was ascribed to microstructural effects on dielectric properties. The SEM images of the fractured surfaces of the pellets are shown in Figs. 5(a) - 5(e), indicating the distributions of the pores inside the pellets. The samples made from the glass powders of large particle sizes were observed to have small pores and low volume fractions of porosity (see Table I); from these results, the samples are expected to have large ϵ values.²⁸⁾

2-3 Conclusions

1. A band-pass filter circuit was designed such that its second harmonic frequency was very sensitive to the dielectric properties of an SL capacitor.
2. The ϵ - SHF correlation shown as a reference curve was established by model simulation based on a circuit, in which various ϵ values and capacitor thicknesses were specified.
3. Using the measured SHF and capacitor thickness, the ϵ values of the capacitors were determined from the ϵ - SHF reference curve. These values were found to be consistent with those of the sintered pellets, prepared with the same glass powders and thermal process as the BPFs.
4. The method of estimating ϵ , from the ϵ - SHF reference curve was demonstrated to be feasible.

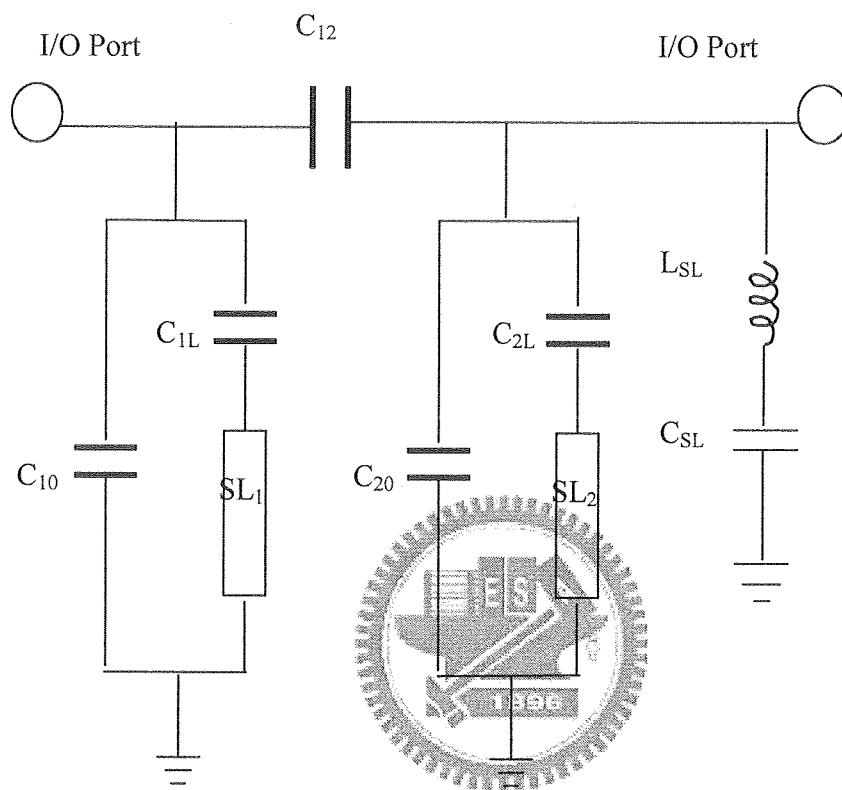


Fig. 1 Equivalent circuit of multilayer BPF, the quarter-wavelength SL is represented by L_{SL} and C_{SL} .

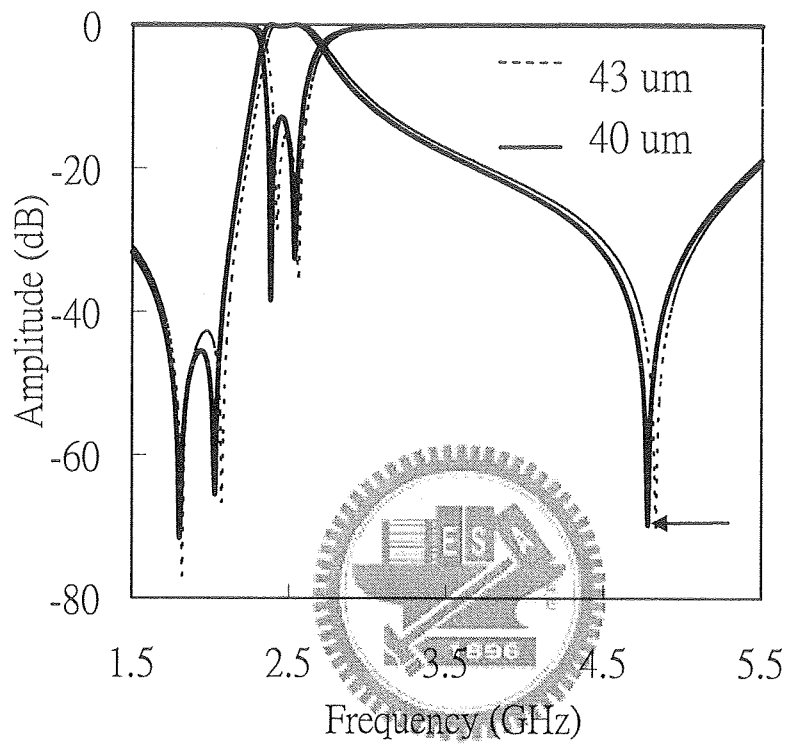


Fig. 2 Typical simulation results for BPF frequency response, obtained using scheme in Fig. 1, where ϵ of SL capacitor was set to be 7.7 and capacitor thickness, 40 and 43 μm . SHF is indicated by an arrow.

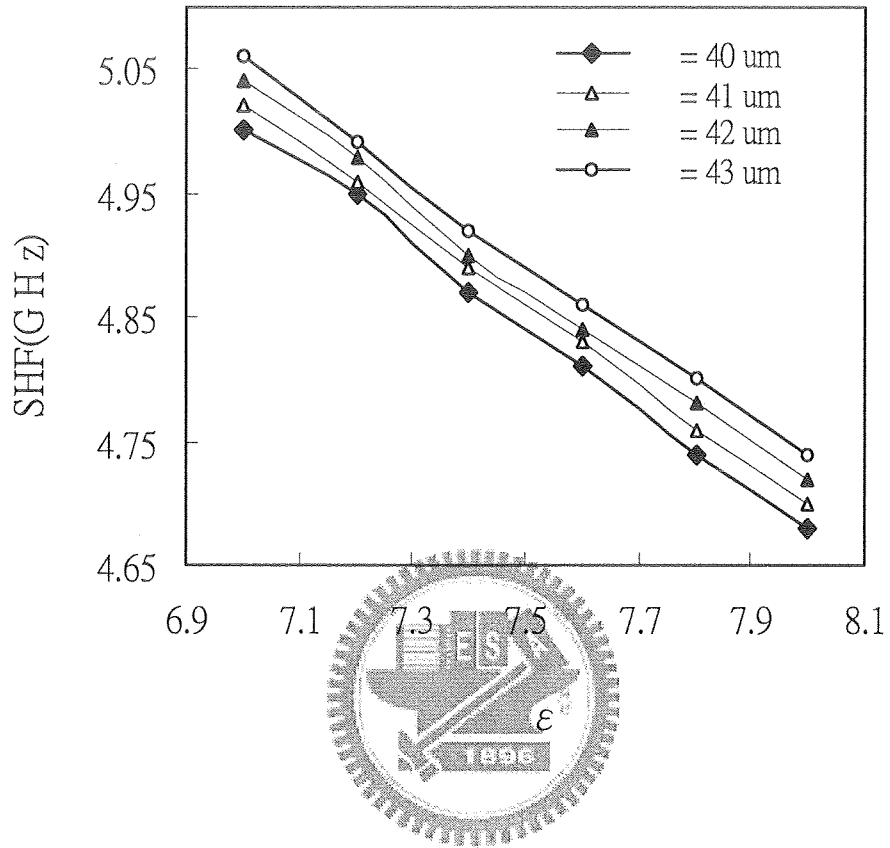


Fig. 3 SHFs obtained by simulation with series of preset dielectric constants ranging from 7.0 to 8.0, for various SL capacitor thicknesses from 40 to 43 μm .

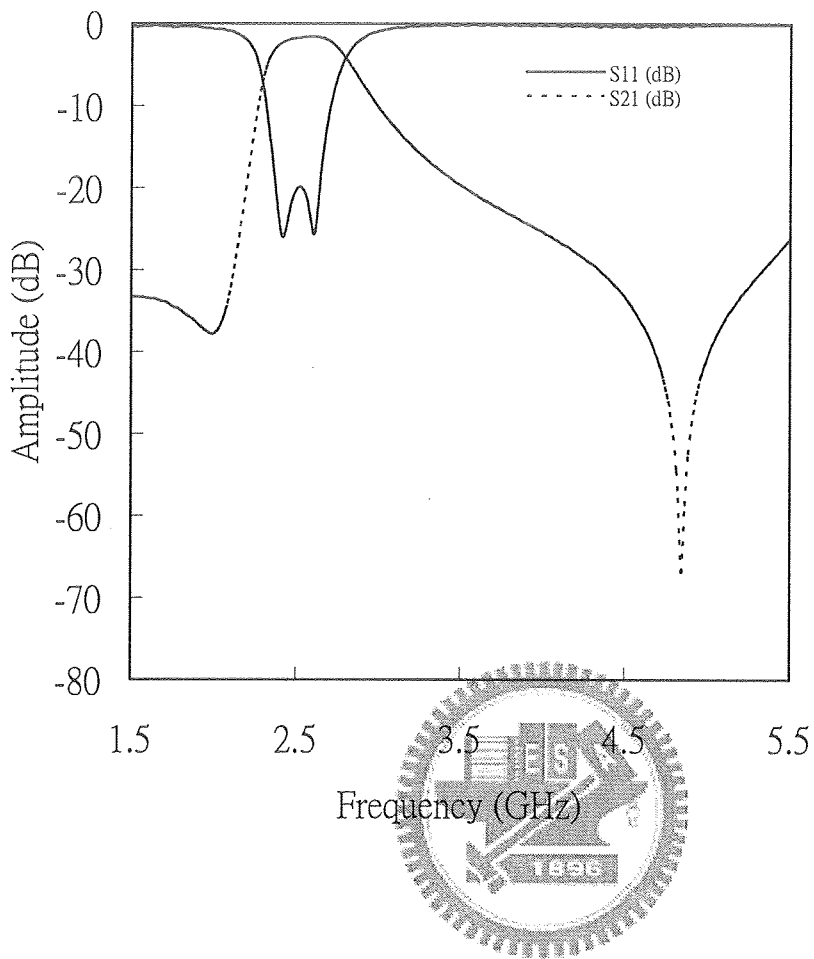


Fig. 4 Typical frequency response spectrum measured from fabricated BPFs.

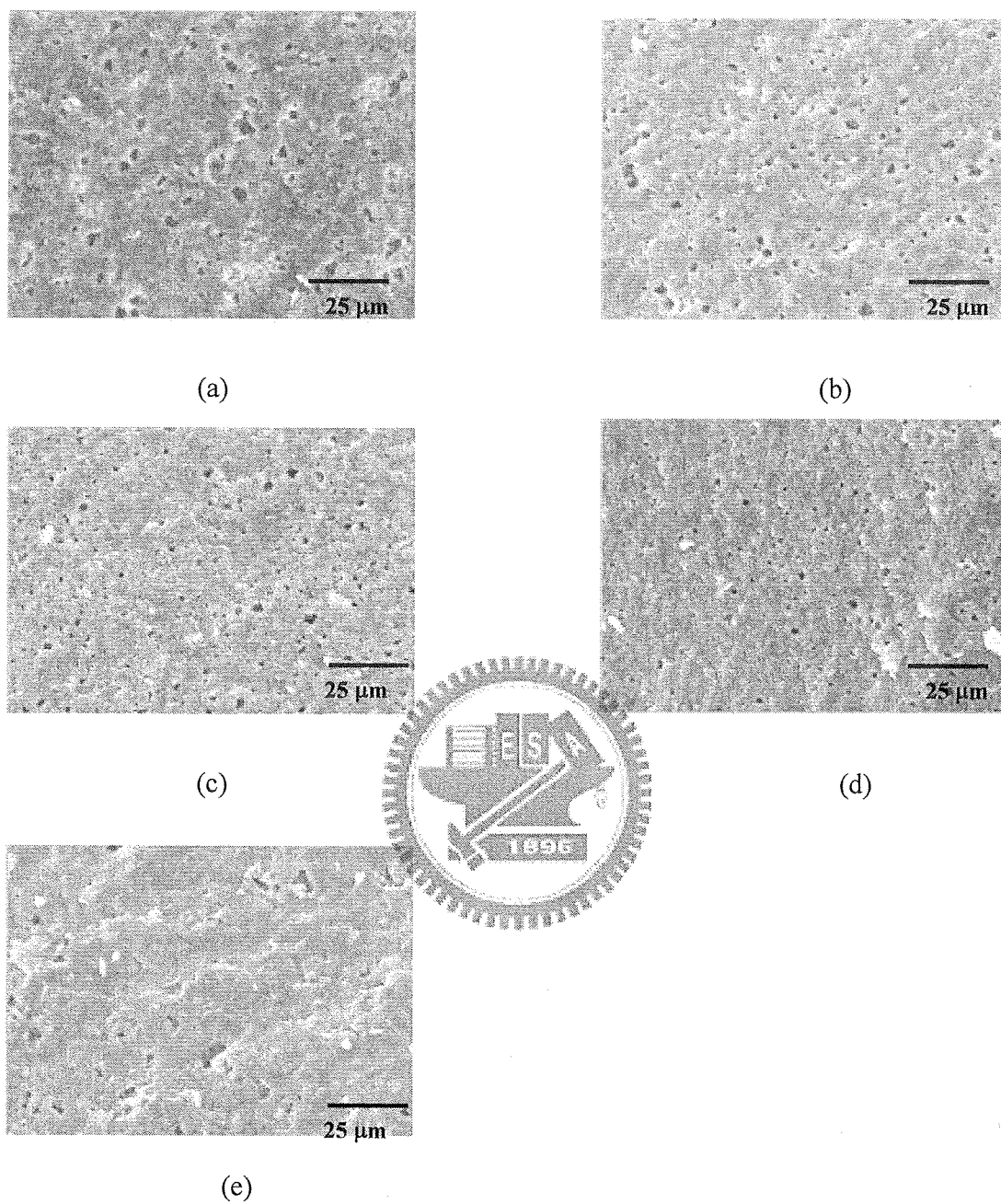


Fig. 5 SEM images of fractured surfaces of pellets made from $\text{BaAl}_2\text{Si}_2\text{O}_8$ glass powders with particle sizes of (a) 2.3, (b) 2.2, (c) 1.6, (d) 1.4, and (e) 1.1 μm .

Table I. (a)-(e). Each subtable shows the particle size of the glass powder, from which the BPFs and pellets were fabricated; it also shows the thickness Δ of the SL capacitors, the SHFs measured from the BPFs, the ε values evaluated from the SHF- ε relationship, the ε_p values measured from the pellets, and pore sizes and porosities measured from the fractured surfaces of the pellets. The accuracy range for SHF is about $\pm 0.17\%$, that for ε is about ± 0.025 and that for ε_p is about ± 0.04 .

<i>(a) Glass particle size=1.3 μm</i>				
Δ (μm)	40	41	42	
SHF (GHz)	4.95	4.96	4.98	
ε	7.20	7.20	7.20	
ε_p / pore size (μm) / porosity (%)	7.21	2.3	10.4	
<i>(b) Glass particle size=1.8 μm</i>				
Δ (μm)	40	41		
SHF (GHz)	4.92	4.94		
ε	7.26	7.25		
ε_p / pore size(μm) / porosity (%)	7.23	2.2	8.3	
<i>(c) Glass particle size=2.2 μm</i>				
Δ (μm)	40	41	42	43
SHF (GHz)	4.90	4.93	4.94	4.96
ε	7.30	7.30	7.30	7.30
ε_p / pore size(μm) / porosity (%)	7.31	1.6	3.5	
<i>(d) Glass particle size=2.7 μm</i>				
Δ (μm)	40	41	42	43
SHF (GHz)	4.88	4.91	4.92	4.93
ε	7.36	7.32	7.35	7.38
ε_p / pore size(μm) / porosity (%)	7.36	1.4	2.6	
<i>(e) Glass particle size=3.8 μm</i>				
Δ (μm)	40	41	42	43
SHF (GHz)	4.77	4.80	4.81	4.83
ε	7.71	7.71	7.71	7.71
ε_p / pore size (μm) / porosity (%)	7.70	1.1	0.4	

Chapter 3 Self-constraining method for low shrinkage

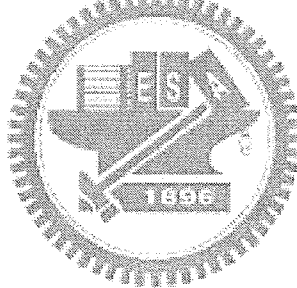
3-1 Experimental procedure

Technical grade SiO_2 (Cerasiv, Germany), CaO (Daiei-Kaikan, Japan), and Na_2O (Daiei-Kaikan, Japan) were used as starting materials for preparing glass powders of CaO-SiO_2 (glass A) and $\text{Na}_2\text{O-CaO-SiO}_2$ (glass B series). In the B series, the composition ratio of CaO to SiO_2 was kept at 1:1, and the fraction of Na_2O was varied from 0.2(B1), 0.5(B2) to 1.0 wt%(B3). The starting material mixtures were ball-milled and then melted in a Pt crucible at 1600 °C for 8 h in an electric furnace to achieve a homogeneous melt. The melt was quenched to prevent crystallization and then milled for 24 h to obtain fine glass powder. The glass particle size was in the range of 3-3.2 μm , as estimated by scanning electron microscopy (SEM). No crystalline phase in the powder was detected by X-ray diffraction (XRD analysis; JSM-5410, JEOL).

Glass A was further mixed with 2 wt% $\text{B}_2\text{O}_3\text{-SiO}_2\text{-Al}_2\text{O}_3\text{-CaO}$ glass

(OST: 602 °C, GP-051, Exojet Corp., Taiwan) as the wetting agent. An appropriate amount of the wetting agent could provide an adhesive force among the glass powder particles in layer A at a temperature above 602 °C, which can enhance the coherency and stability of the glass-powder structure and cause no shrinkage in layer A. Thus, layer A could exert a coherent constraining effect on the layer B series. To prepare the layer A and B series, an organic vehicle for the glass powder consisting of a binder, a plasticizer, and solvents was used in the casting slurries. The green layer A and B series were uniform in thickness at 45 μ m and 15 μ m, respectively. The OST of each kind of glass layer was measured using a thermal mechanical analyzer (TMA; DIL-402EP, NETZSCH), where the tested samples consisted of 16 identical layers laminated together. The same equipment was used to carry out the shrinkage test. The phases of the crystallized glass after the OST measurement were identified by X-ray diffraction analysis. The thermal reaction of the glass crystallization was monitored by differential thermal analysis (DTA; STA 409PC, Netzsch).

The samples for the shrinkage test were prepared with eight CTs laminated at 2760 N/cm^2 and $70 \text{ }^\circ\text{C}$ for 10 min, where the CTs were made of layer A and one of the B series. For comparison, samples made solely of laminated A layers were also tested. The above samples, labeled A/B1, A/B2, A/B3 and A, were cut into $10 \times 10 \text{ mm}$ pieces and sintered in the TMA following two thermal profiles(Fig. 9(a)-(b)). The dielectric constant of the sintered samples was measured using HP8719D at 100 MHz .



3-2 Results and discussion

The measured shrinkage curves (along x/y direction) for individual tape, A and B series showing their OSTs are shown in Fig. 6. The tests were carried out at a heating rate of 3°C/min. OST showed a decrease with increasing fraction of Na₂O. This dependence is summarized in Table II. The corresponding DTA curves (Fig. 7, carried out at 10 °C /min) for these glasses showed the occurrence of crystallization. For each glass the crystallization temperature (CRT) is higher than the OST, but both have similar trends when Na₂O content was varied. The CRT results are also listed in Table II.

The OST of tape A (802 °C) was found higher than the OSTs and CRTs of B2 and B3, that allowed tape A to serve as the constraining layer for B2 and B3 until the latter forms a solid frame that resists shrinkage on their own. However, the OST of tape A appeared lower than the CRT of B1 (810 °C). Tape A became soft when tape B has not formed the solid frame yet, which made it impossible

for tape A to apply effective constraining on B1 beyond 802 °C. Therefore, we would not expect low shrinkage for the composite tape A/B1 after sintering.

The phases of the crystallized glass after the OST measurement were identified by X-ray diffraction analysis. Typical results shown in Fig. 8 indicate that the crystalline phase was $\text{Ca}_3\text{Si}_3\text{O}_9$.

For the test on the shrinkage behavior of samples A/B1, A/B2, A/B3 and A, two sets of thermal profiles I and II were adopted in the TMA, as shown in Figs. 9(a) and 9(b). They have the same heating rate of 3 °C/min and a constant-temperature duration at 400 and 880 °C except that profile I has an extra constant-temperature duration for 2 h at 650 °C. The resulting shrinkage as shown in Table III shows a strong dependence on Na_2O content and profile pattern.

Samples A exhibited a shrinkage of 13% , typical of the LTCC devices after sintering without external constrain. Samples A/B1 did not show much improvement on shrinkage reduction, as discussed

above. Samples A/B2 following the sintering profile I shown a remarkably low shrinkage behavior (0.2%). However, profile II did not show a similar result to the samples A/B2. The difference was ascribed to the shortage of sintering time in profile II that would not allow the complete softening and recrystallization tape B2 before the OST of tape A.

Samples A/B3 showed a significant amount of shrinkage in both profiles I and II. The failure of the constraining effect of tape A on B3 was due to the fact that the OST of B3 (606 °C) is very close to that of the wetting agent ($B_2O_3-SiO_2-Al_2O_3-CaO$ glass, OST=602 °C) in tape A. With the heating rate of 3 °C/min in the profiles, B3 would start to soften and shrink approximately 1 min later than the wetting agent. The latter, in such an early stage of softening, would not fully exert an adhesive force among the glass powders of layer A. Therefore, tape A failed to constrain sample B3 in the samples A/B3 in this temperature range. The shrinkage curves of samples A/B2 and A/B3 heated in profile I are shown in Fig. 10 indicating that a significant shrinkage of A/B3

along the x/y-direction indeed started at a heating temperature of approximately 606 °C, while those of A/B2 indicated a negligible shrinkage in all the test temperature range.

The microstructure observed by SEM on the A/B2 sample surface (with thermal etching) is displayed in Fig. 11 showing crystallized grains with an average size of 1.2 μm. The fractured cross section of the sample (Fig. 12) revealed an internal structure with crystallized grains and a sodium element distribution in tape B2 (EDS image of Na). The results of the dielectric constant measurement of the sintered samples (Table IV) showed that shrinkage actually has no effect on the dielectric properties. The longer sintering time in the heating profile I than that in profile II increased the dielectric constant, apparently due to the better crystallization of the samples.

3-3 Conclusions

1. The onset shrinkage temperature could be tuned by adjusting the amount of Na_2O added to the CaO-SiO_2 glass.
2. The onset shrinkage and crystallization temperatures of the two glass layers as well as the heating profile had a strong effect on the shrinkage ratio along the x/y direction of the laminated samples.
3. The lowest shrinkage ratio after sintering up to $880\text{ }^\circ\text{C}$ was found to be 0.2%. The large variation of shrinkage ratio of the sintered samples does not have a significant effect on their dielectric properties.

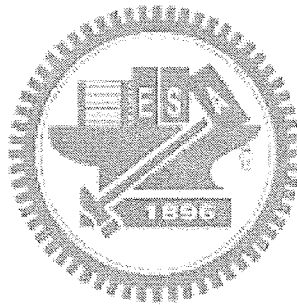
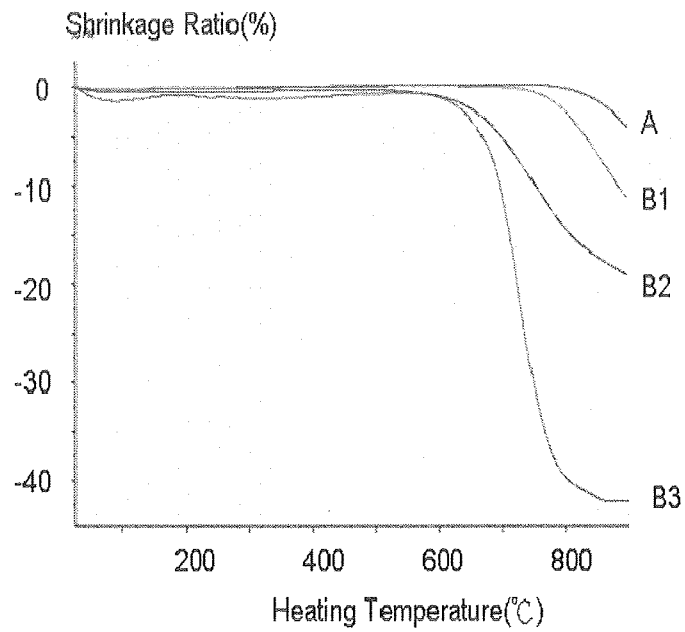


Fig. 6 Measured linear shrinkage ratio along plane of individual tape A and B series heated in thermal mechanical analyzer at heating rate of 3°C/min, showing onset shrinkage temperature (OST) of each glass.

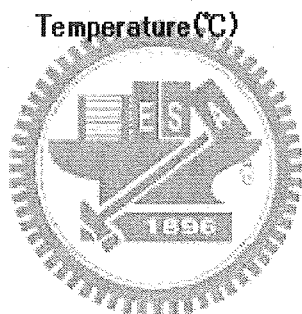
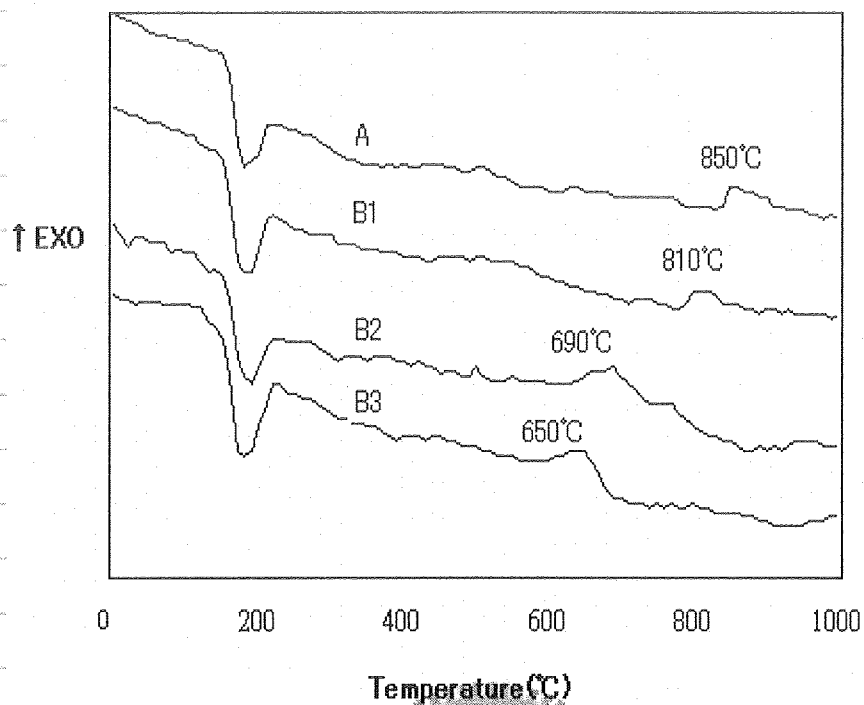


Fig. 7 Differential thermal analysis of glasses A and B series carried out at 10°C /min, showing temperature of crystallization of each glass.

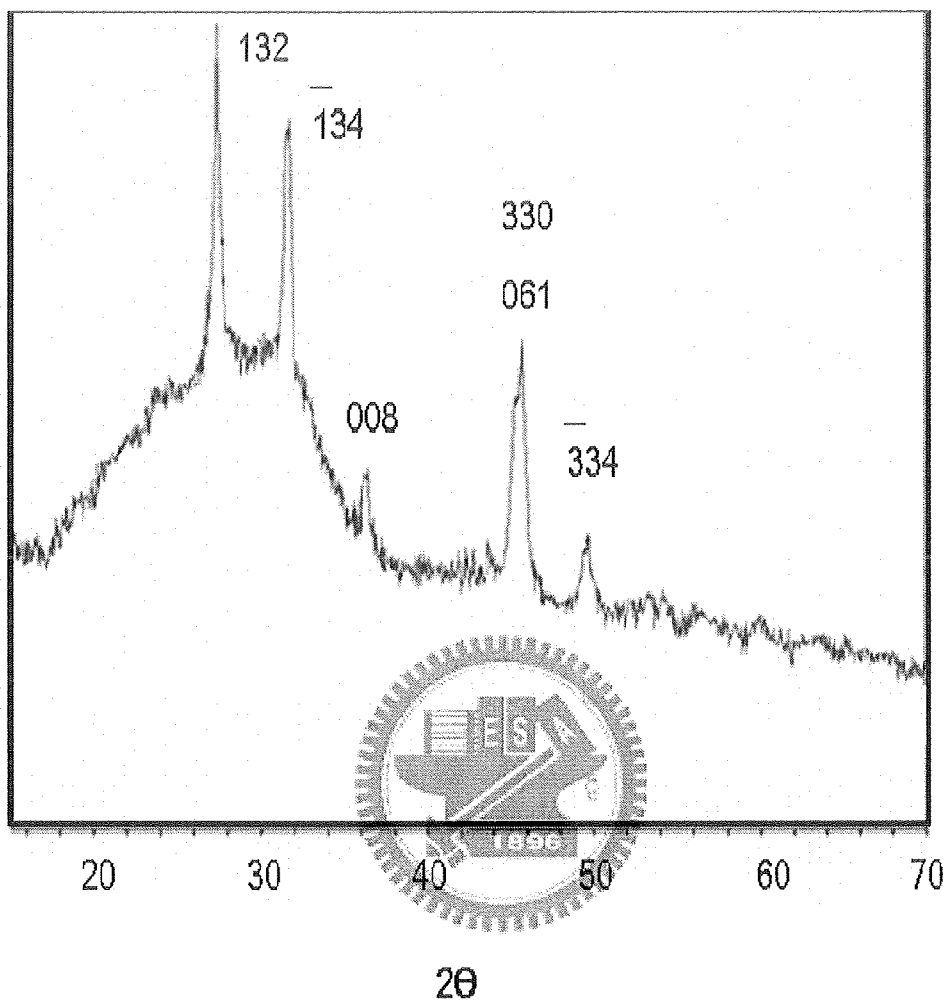


Fig. 8 Typical x-ray diffraction results of the crystallize glass A and B series, indicating crystalline phase $\text{Ca}_3\text{Si}_3\text{O}_9$.

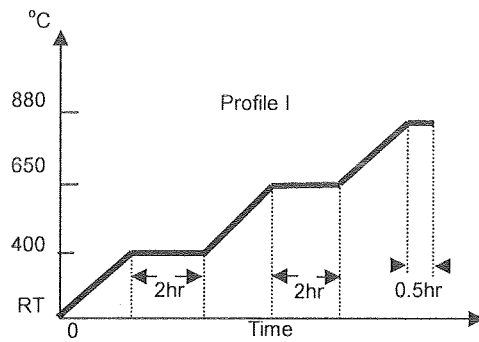


Fig. 9(a)

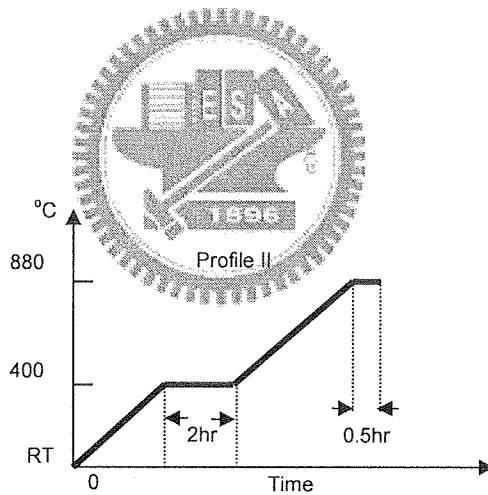


Fig. 9(b) Two sets of thermal profiles I (9a) and II (9b) adopted in the TMA for the test of the shrinkage behavior of samples A/B1, A/B2, A/B3 and A. They have the same heating rate of 3°C/min but I has an extra constant-temperature duration at 650 °C.

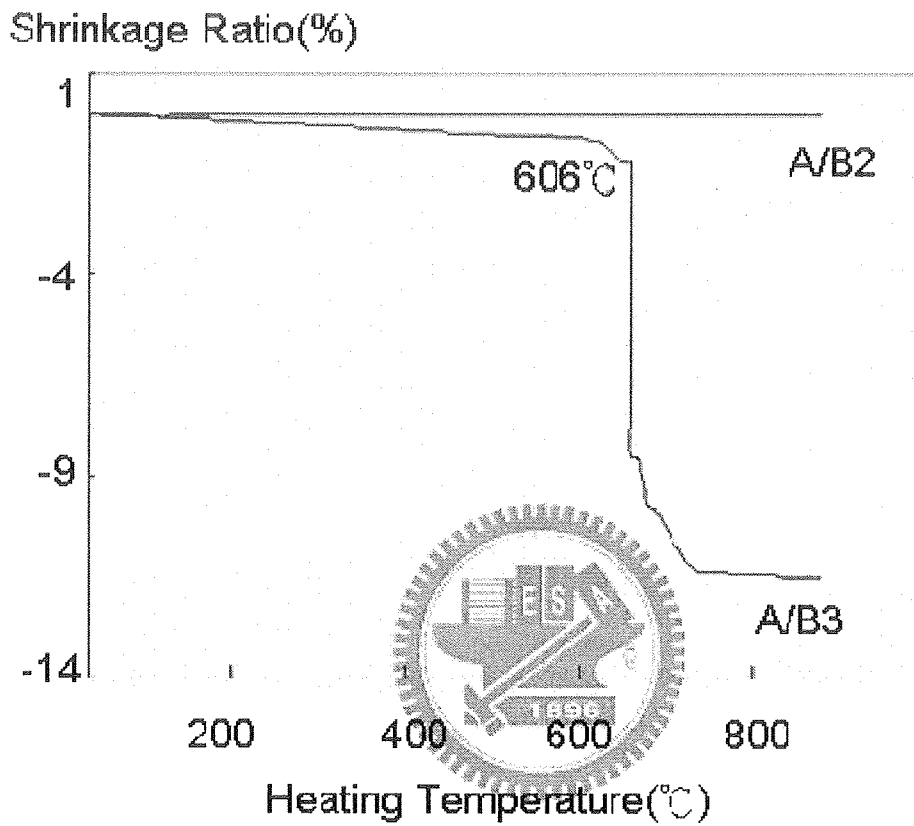


Fig. 10 Shrinkage curves of samples A/B2 and A/B3 heated using profile I, showing total shrinkage of A/B2 of only 0.2%.

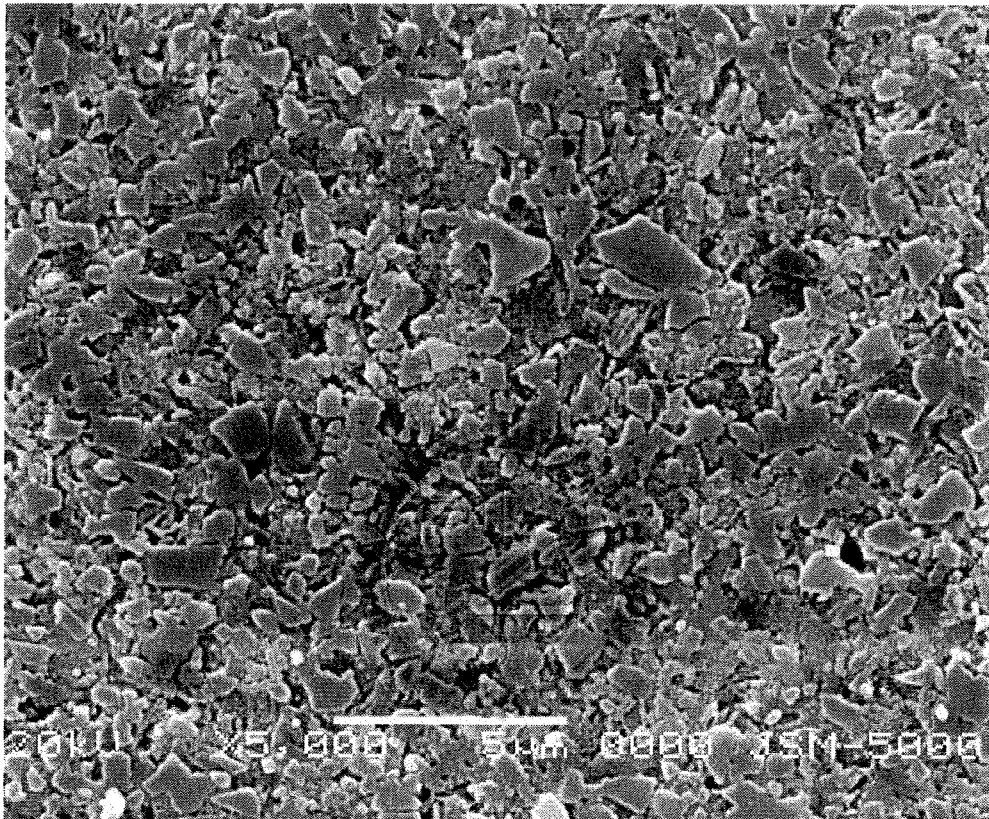


Fig. 11 Microstructure observed by SEM on A/B2 sample surface with thermal etching treatment, showing crystallized grains of 1.2 μm average size.

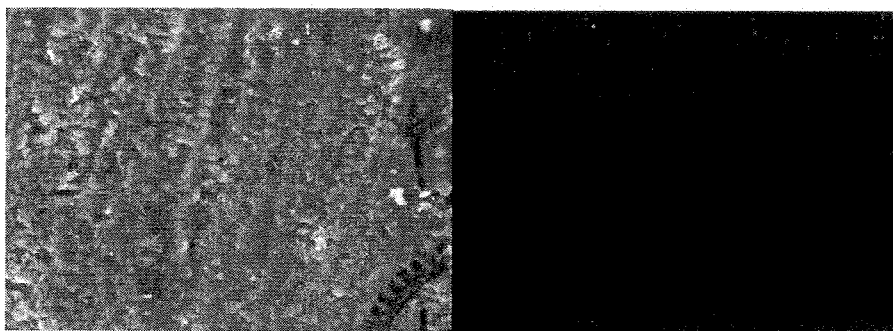


Fig. 12 Fractured cross section of sample A/B2 and associated EDS image, revealing crystallized grains in internal structure and sodium element (gray spots) distribution in tape B2.

Table II. Onset shrinkage temperatures and crystallization temperatures of CaO-SiO₂ glass layers with different Na₂O contents.

Glass layer	A	B1	B2	B3
Na ₂ O content (wt%)	0	0.2	0.5	1.0
Onset shrinkage temperature (°C)	802	756	638	606
Crystallization temperature (°C)	850	810	690	650

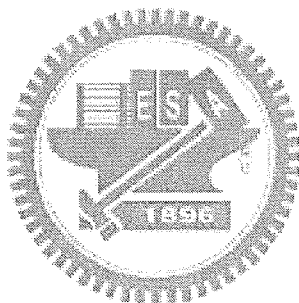


Table III. Shrinkage ratios of composite tapes made of glass layers A and B series sintered in profiles I and II.

Sample	A	A/B1	A/B2	A/B3
Profile I (%)	13	7	0.2	11
Profile II (%)	13	11	6	11

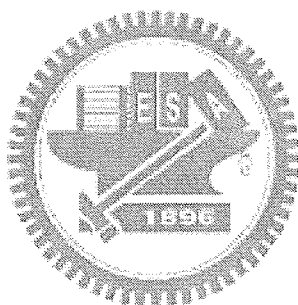
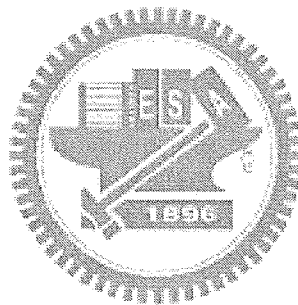


Table IV. Dielectric constants of composite tapes made of glass layers A and B series sintered in profiles I and II.

Sample	A	A/B1	A/B2	A/B3
Profile I	6.02	6.00	6.01	6.00
Profile II	5.92	5.91	5.93	5.90



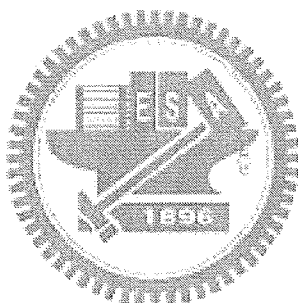
Chapter 4 Characterization of inductor with Ni-Cu-Zn ferrite embedded in B₂O₃-SiO₂ glass

4-1 Experimental procedure

In this study, Ni-Cu-Zn ferrite (NA-120, Nakagawa, Japan) and B₂O₃-SiO₂ glass (MLS-25M, NEG, Japan) were used as inductor layer and LTCC substrate, respectively. They have average particle size of 1.24 μm and 2.42 μm, respectively, based on the measurement using Horiba 910. The ferrite contains 44.6% of Fe, 16.63% of Ni, 3.00% of Cu, 12.39% of Zn, and 0.8% of Bi, and the glass consists of 3.79% of B, 21.47% of Si, and 4.33% of Al, and 0.71% of K. Different amounts of Bi₂O₃ (PCF-Climie, France) was used as flux to reduce the sintering temperature of Ni-Cu-Zn ferrite, though a small quantity of Bi₂O₃ has already been contained in the original ferrite powder. Also, to match the sintering shrinkage with ferrite, different amounts of Al₂O₃ (Showa Denko, Japan) was added to retard the early sintering of the B₂O₃-SiO₂ glass.

Various powders were mixed using ball milling for 24h and then dried at 120°C. The powders were mixed with an organic vehicle to form slurry. Green tapes of both Ni-Cu-Zn ferrite and B₂O₃-SiO₂ glass were fabricated using a doctor blade tape caster. Ni-Cu-Zn ferrite ink was made from the powder with the addition of organics. The chip inductors with six-layer coil were made according to the structure indicated in Fig. 13. Silver conductor (Shoie Inc., Japan) was adopted as the material for printed coil on the B₂O₃-SiO₂ glass. The printed silver coils on six various tapes of B₂O₃-SiO₂ glass were connected through vias. The width of conductor is 95 μm, and the inductor is 2.0 mm by 1.2 mm. Ni-Cu-Zn ferrite was inserted in the core of the spiral silver coils by punching circular cavity on the B₂O₃-SiO₂ glass tape and subsequently filled with Ni-Cu-Zn ferrite paste. Ni-Cu-Zn ferrite tapes were utilized for the cap and the bottom of the chip. Tapes of Ni-Cu-Zn ferrite and B₂O₃-SiO₂ glass were laminated together at 80°C for 20 min under the pressure of 3000 psi and then co-fired using the profile indicated in Fig. 14. The microstructures of the multilayer

ceramic were examined using scanning electron microscopy (SEM, JSM5410, JEOL). Magnetic properties of the inductors were examined using an HP 4291A impedance analyzer at the frequency range from 1MHz to 25 MHz.



4-2 Results and discussion

A Ni-Cu-Zn ferrite doped with Bi_2O_3

Fig. 15 shows the shrinkages of Ni-Cu-Zn ferrite doped with various amounts of Bi_2O_3 . It indicates that a higher amount of Bi_2O_3 produces a larger shrinkage at the same sintering temperature. Addition of Bi_2O_3 in ceramics generally lowers the required activation energy for sintering and therefore enhances the densification¹⁹⁾. The onset temperatures of densification and the resultant residual porosities for Ni-Cu-Zn ferrite with various amounts of Bi_2O_3 addition are shown in Table V. The onset densification temperature of Ni-Cu-Zn ferrites reduces from 792 to 727 °C as the Bi_2O_3 addition raised from 0 to 2wt%. It is evident that Bi_2O_3 addition significantly improves the densification of Ni-Cu-Zn ferrites²⁷⁻²⁹⁾. At the sintering temperature of 860 °C, the residual porosity for Ni-Cu-Zn ferrites with 0 and 2wt% Bi_2O_3 additions are 10.2% and 1.2%, respectively. A higher residual porosity present generally causes a larger demagnetizing effect. SEM micrographs of Ni-Cu-Zn ferrites with various amounts of Bi_2O_3

additions are shown in Fig. 16 and the calculated average grain sizes are listed in Table V. The grain size of the specimen generally reduces with Bi_2O_3 content. A fine grain size of $0.38 \mu\text{m}$ for Ni-Cu-Zn ferrite with 2wt% of Bi_2O_3 was obtained, which is significantly lower than that of the pure Ni-Cu-Zn ferrite ($1.24 \mu\text{m}$). The results are consistent with those observed by Chen et al (30, 31).

Permeability (μi) versus frequency curves for Ni-Cu-Zn ferrite with various amounts of Bi_2O_3 addition and sintered at 860°C are shown in Fig. 17. Permeability of ferrite increases with the Bi_2O_3 content, which strongly correlated to the sintered densities of the ferrites. For instance, permeability (μi) of 86 and quality factor (Q) of 492 were obtained for ferrite specimens with 2wt% Bi_2O_3 addition at 3MHz. They are significantly improved compared with those of ferrite without Bi_2O_3 addition (μi : 64 and Q: 11), as indicated in Table I. Ni-Cu-Zn ferrites with 2wt% of Bi_2O_3 addition was thus selected for the co-firing experiment based on its satisfied densification, micro-structural evolution and

magnetic properties.

B. B_2O_3 - SiO_2 glass with Al_2O_3 addition

Generally the onset temperatures of the pure glasses are significantly lower than those of ferrites. In order to retard the early shrinkage, various amounts of Al_2O_3 addition were added into the B_2O_3 - SiO_2 glass. Fig. 18 showed that the densification of B_2O_3 - SiO_2 glass with various amounts of Al_2O_3 addition. Shrinkage of the B_2O_3 - SiO_2 glass-ceramic is decreases with increasing Al_2O_3 content. At the sintering temperature of 900 °C, the shrinkages for pure B_2O_3 - SiO_2 glass and 45% Al_2O_3 added B_2O_3 - SiO_2 glass-ceramic are 44% and 2%, respectively. Carefully examine the results shown in Fig. 18, the sintering shrinkage profile of the 35% Al_2O_3 added B_2O_3 - SiO_2 glass-ceramic (10%) is similar to that of the Ni-Cu-Zn ferrite with 2wt% of Bi_2O_3 addition (14%). The sintering shrinkage mismatch is insignificant if they were co-fired at the temperature of 860 °C, at which the shrinkages for glass-ceramic

and ferrite are 10% and 14%, respectively.

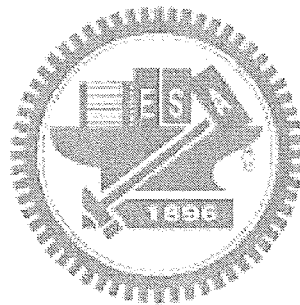
C. Material compatibility between Ni-Cu-Zn ferrite and B_2O_3 - SiO_2 glass

Before inserting the ferrite layer (Bi_2O_3 doped Ni-Cu-Zn ferrite) into B_2O_3 - SiO_2 glass substrate, a material compatibility study was performed in order to minimize the sintering stress due to shrinkage mismatch. SEM micrographs of 2 wt% Bi_2O_3 added Ni-Cu-Zn ferrite co-fired with B_2O_3 - SiO_2 glass with various amounts of Al_2O_3 addition at 860 °C is given in Fig. 19. Pure B_2O_3 - SiO_2 glass begins to shrink rapidly at 700 °C, at which the shrinkage of the Bi_2O_3 added Ni-Cu-Zn ferrite is trivial. The sintering mismatch leads to camber in the co-fired structures due to unbalance stress. After tailoring the composition, the sintering shrinkage of the Ni-Cu-Zn ferrite fluxed with 2 wt% Bi_2O_3 almost identical to that of 35 wt% Al_2O_3 added B_2O_3 - SiO_2 glass-ceramic. Neither cracking nor delamination is evident in the interface between these two

dissimilar layers (Fig. 20 a). On the contrary, pure B_2O_3 - SiO_2 glass is not compatible with Ni-Cu-Zn ferrite (Fig. 20 b), which induces cracks along the interface.

Frequency dependences of the inductance and quality factor for the inductor with embedded spiral coils are showed in Fig. 21. The change of the inductance in the frequency ranging between 1MHz and 25MHz is insignificant. For the inductor with 35% Al_2O_3 added B_2O_3 - SiO_2 glass-ceramic, the inductance and quality factor are about 57 nH and 10 (measured at 25MHz), respectively. However, for the inductor having a structure of 2wt% Bi_2O_3 added Ni-Cu-Zn ferrite buried within the core of the spiral silver coil in the 35% Al_2O_3 added B_2O_3 - SiO_2 glass-ceramic, the inductance and quality factor are about 138 nH and 17 (measured at 25MHz), respectively. It is obvious that Ni-Cu-Zn ferrite buried in B_2O_3 - SiO_2 glass-ceramic can raise the inductance and quality factor values. The higher inductor value of the LTCC structure is due to the existence of ferrite material that has a higher permeability compared with that of pure glass-ceramic. The higher quality

factor is due to the glass-ceramic with embedded ferrite structure shifts the electromagnetic resonance to a lower frequency.



4-3 Conclusions

1. The addition of Al_2O_3 into $\text{B}_2\text{O}_3\text{-SiO}_2$ glass can delay the onset temperature of sintering.
2. The sintering temperature of Ni-Cu-Zn ferrite was reduced using the sintering aid of Bi_2O_3 .
3. A compatible system for 2wt% Bi_2O_3 added Ni-Cu-Zn ferrite co-fired with 35% Al_2O_3 added $\text{B}_2\text{O}_3\text{-SiO}_2$ glass-ceramic was obtained.
4. Inserting the Ni-Cu-Zn ferrite into the $\text{B}_2\text{O}_3\text{-SiO}_2$ glass within the spiral silver coil, can increase the inductance and quality factor of the device.



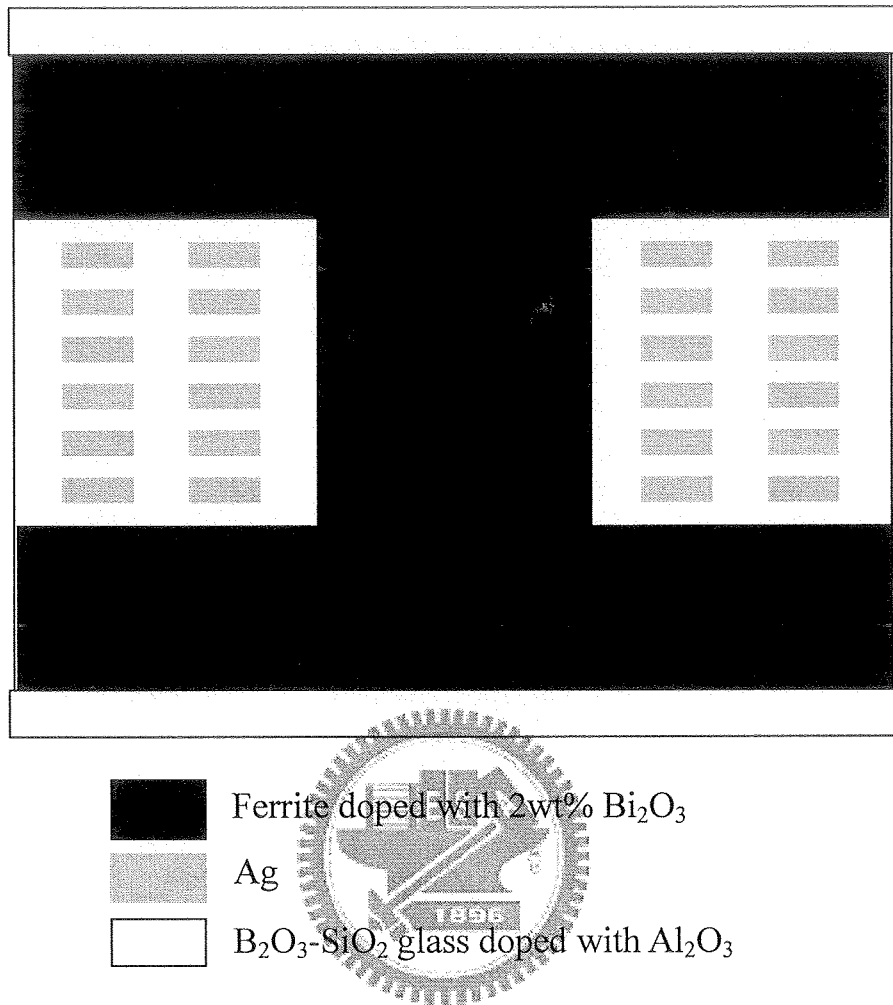


Fig. 13 Design of chip inductors with six-layer coil

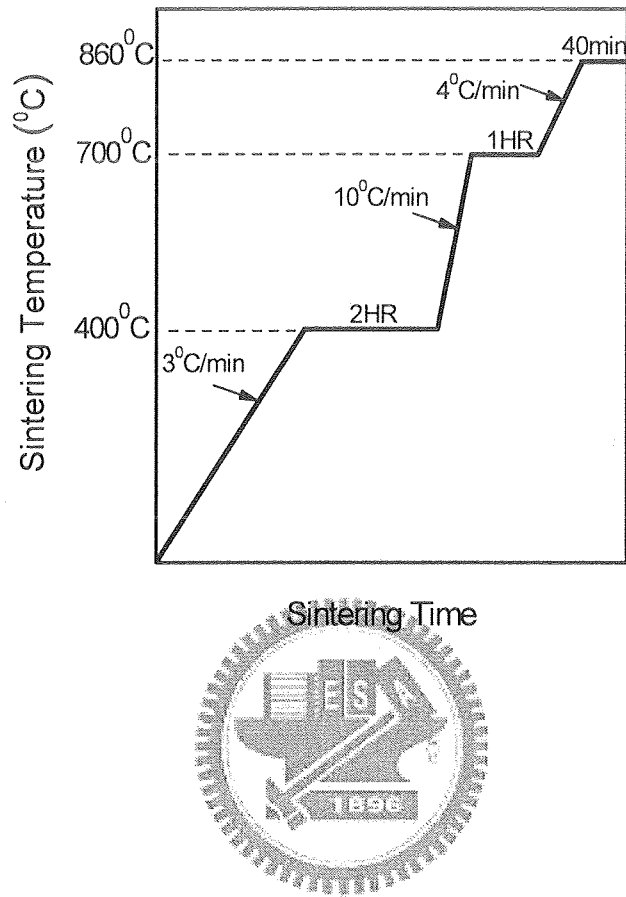


Fig. 14 Sintering profile for the inductor

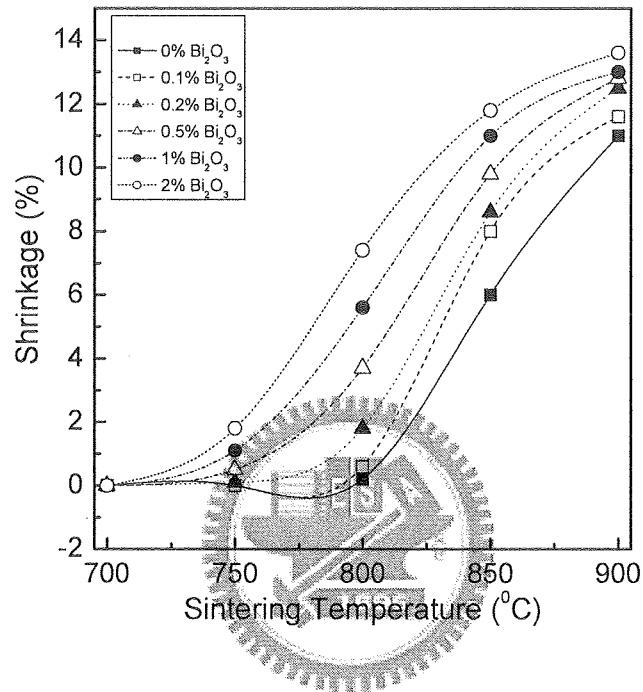


Fig. 15 Sintering shrinkages of Ni-Cu-Zn ferrites with various amounts of Bi₂O₃ additions

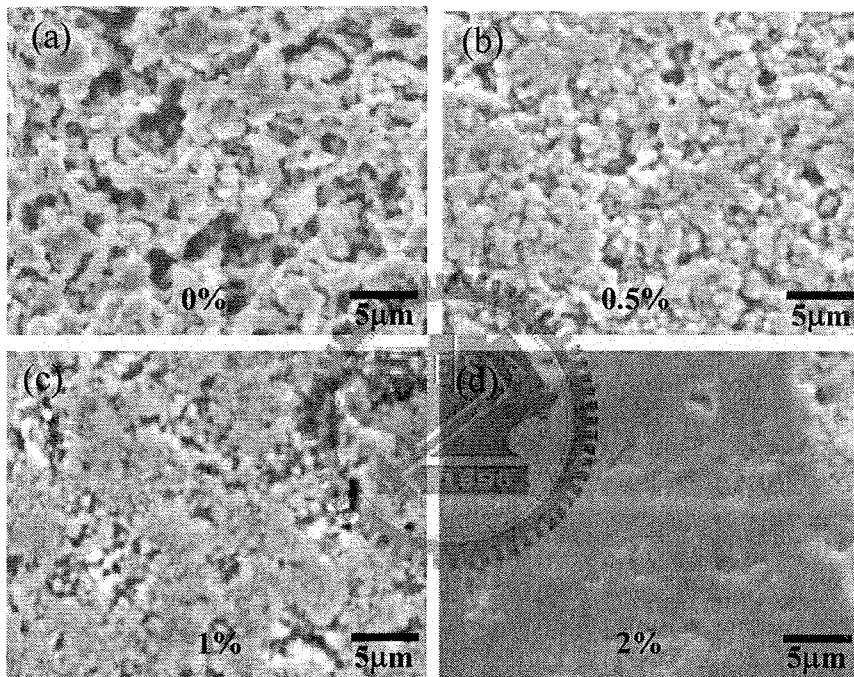


Fig. 16 SEM micrographs of Ni-Zn-Cu ferrites sintered with various amounts of Bi₂O₃ additions.

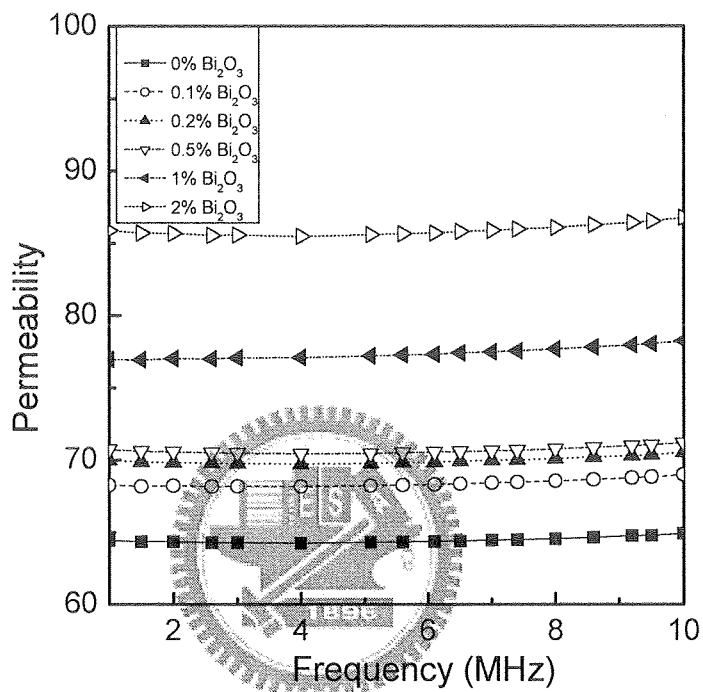


Fig. 17 Permeability versus frequency curves for Ni-Cu-Zn ferrite with various amounts of Bi₂O₃ addition and sintered at 860 °C.

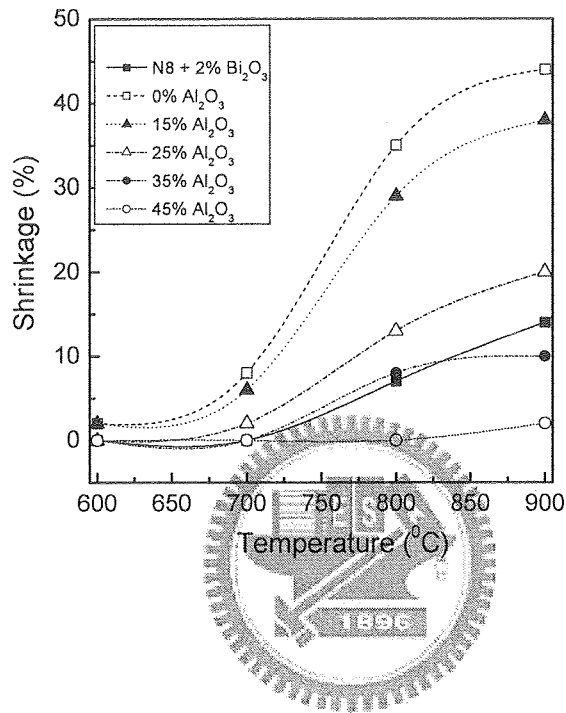


Fig. 18 Sintering shrinkages of B₂O₃-SiO₂ glass with various amounts of Al₂O₃ addition.

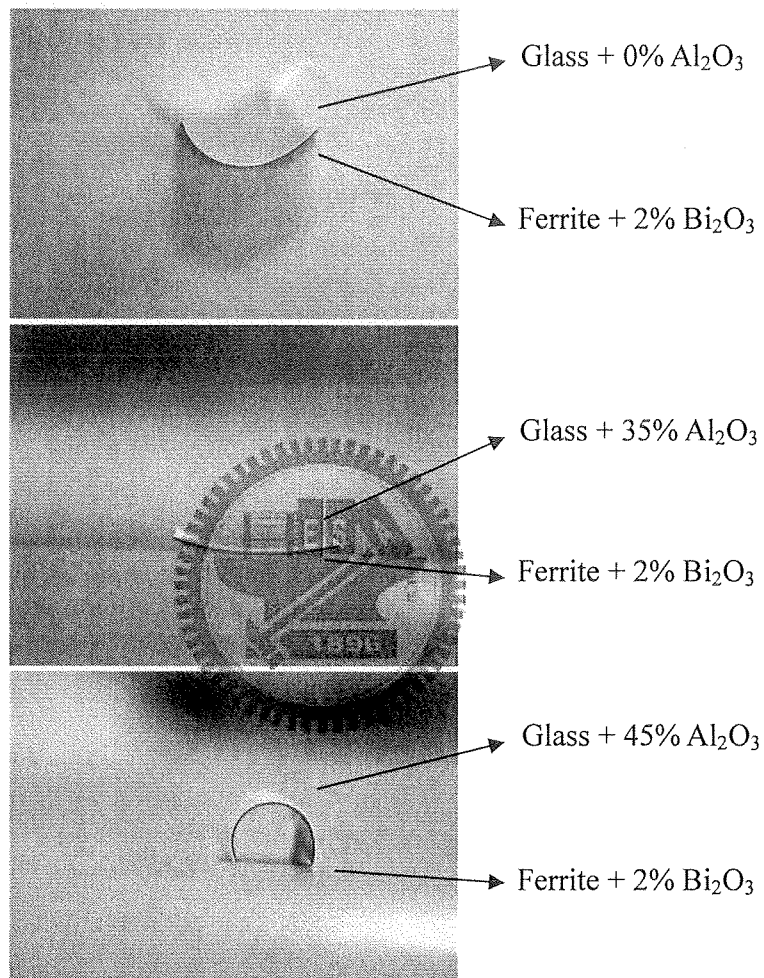
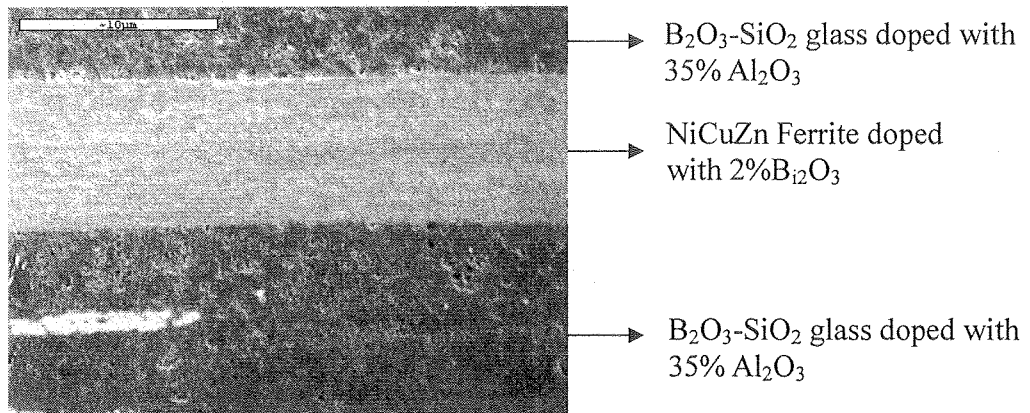
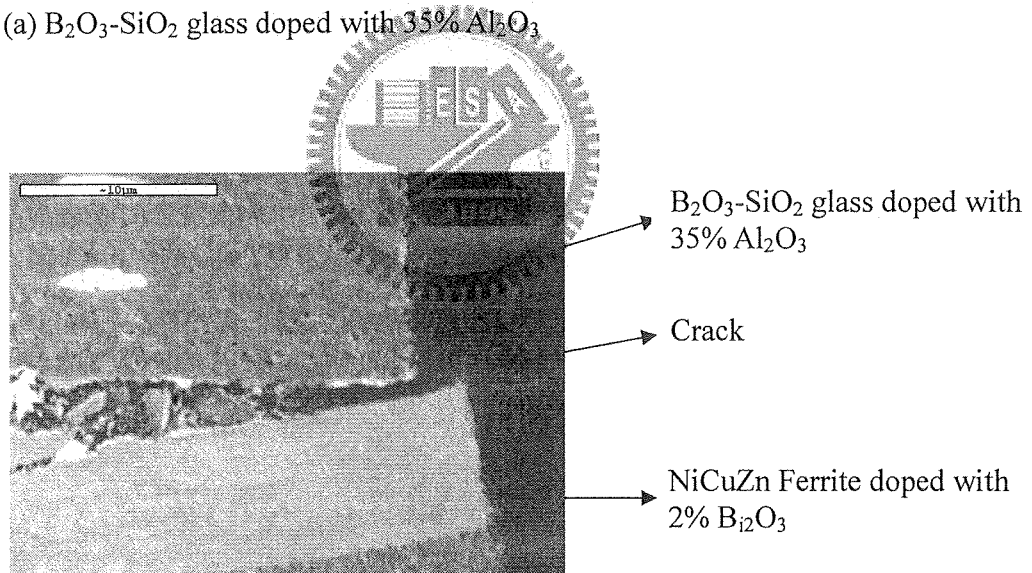


Fig. 19 SEM micrographs of 2 wt% Bi₂O₃ added Ni-Cu-Zn ferrite co-fired with B₂O₃-SiO₂ glass with various amounts of Al₂O₃ addition at 860 °C.



(a) B₂O₃-SiO₂ glass doped with 35% Al₂O₃



(b) B₂O₃-SiO₂ glass doped with 0% Al₂O₃

Fig. 20 Sintering compatibility study of the Ni-Cu-Zn ferrite and B₂O₃-SiO₂ glass

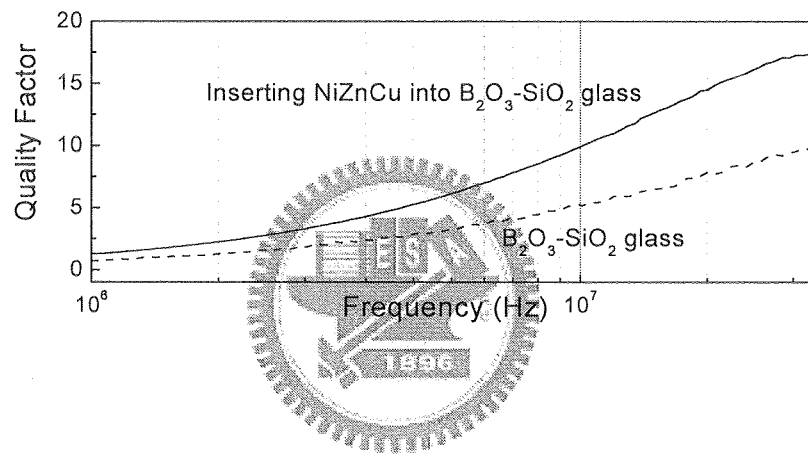
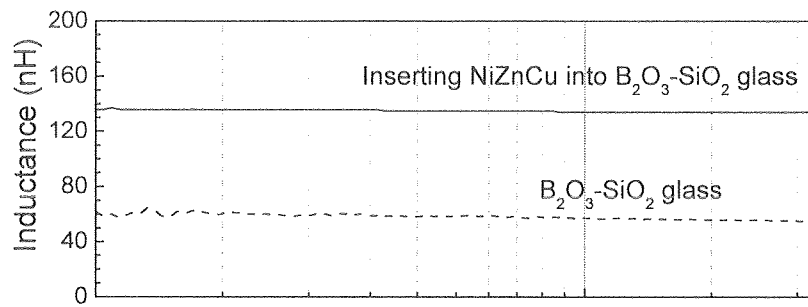
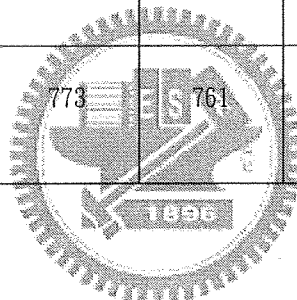


Fig. 21 Frequency dependences of the inductance and quality factor for the inductor with embedded spiral coils

Table V Characteristics of the Ni-Cu-Zn ferrite with various amounts of Bi₂O₃ additions

	Ni-Cu-Zn ferrite with various amounts of Bi ₂ O ₃ additions					
	0%	0.1%	0.2%	0.5%	1%	2%
Permeability (3MHz)	64	68	70	71	77	86
Q value (3MHz)	11	12	30	34	71	492
Pore Size (μm)	0.9	0.89	0.72	0.68	0.55	0.38
Porosity (%)	10.2	8.9	6.3	4.6	3.1	1.2
Onset temperature of shrinkage (°C)	792	773	761	742	738	727



Chapter 5 Summary

1. The proposed method of estimating the dielectric properties of the dielectric layers in low-temperature-cofired ceramic devices was verified in this study. A band-pass filter circuit was designed such that its second harmonic frequency was very sensitive to the dielectric properties of an SL capacitor. The ϵ - SHF correlation shown as a reference curve was established by model simulation based on a circuit, in which various ϵ values and capacitor thicknesses were specified. Following the same design, real BPFs were fabricated with $\text{BaAl}_2\text{Si}_2\text{O}_8$ glass powders of various particle sizes to achieve different dielectric properties of their capacitors. Using the measured SHF and capacitor thickness, the ϵ values of the capacitors were determined from the ϵ - SHF reference curve. These values were found to be consistent with those of the sintered pellets, prepared with the same glass powders and thermal process as the BPFs. The method of estimating ϵ , from the ϵ - SHF reference curve was demonstrated to be feasible. This new

method may find practical applications in estimating the ϵ values of the dielectric layers in other low-temperature-cofired multilayered ceramic devices, in which the same dielectric layers used in the SL capacitors of BPFs were fired as dummy samples along with the devices.

2. The proposed new technique of low-shrinkage LTCC based on a self-constraining mechanism was verified in this study. The green tapes used in this technique composed of two laminated glass layers, each of which has distinct onset shrinkage temperature. The onset shrinkage temperature could be tuned by adjusting the amount of Na_2O added to the CaO-SiO_2 glass. Each layer works as a constraining layer to the other layer in distinct temperature range. The onset shrinkage and crystallization temperatures of the two glass layers as well as heating profile had strong influence on the shrinkage ratio along the x/y direction of the laminated samples. The lowest shrinkage ratio after sintering up to 880°C was found to be 0.2%. The large variation of shrinkage ratio of the sintered

samples does not have a significant effect on their dielectric properties.

3. Pure Ni-Cu-Zn ferrite is incompatible with $B_2O_3-SiO_2$ glass during co-firing process, due to the sintering shrinkage mismatch. The addition of Al_2O_3 into $B_2O_3-SiO_2$ glass can delay the onset temperature of sintering. Also, the sintering temperature of Ni-Cu-Zn ferrite was reduced using the sintering aid of Bi_2O_3 . A compatible system for 2wt% Bi_2O_3 added Ni-Cu-Zn ferrite co-fired with 35% Al_2O_3 added $B_2O_3-SiO_2$ glass-ceramic was obtained. Inserting the Ni-Cu-Zn ferrite into the $B_2O_3-SiO_2$ glass within the spiral silver coil, can increase the inductance and quality factor of the device.

Reference

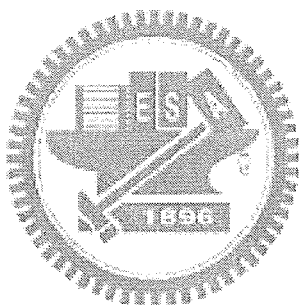
- 1) Y. L. Low and R. C. Frye: IEEE Multi-Chip Module Conference (MCMC' 97), (1997) p. 27.
- 2) A. B. Frazier, R. O. Warrington, and C. Friedrich: IEEE Trans. on Indus. Elec., vol. 42, (1995) p. 423.
- 3) A. Matsuzawa: IEEE Trans. on Microwave Theory and Techniques, vol. 50, (2002) p. 245.
- 4) K. L. Tai: Proceedings of the Asia and South Pacific Design Automation Conference (ASP-DAC), (2000) p. 211.
- 5) J. S. Lim and D. C. Park: IEEE Trans. on Microwave Theory and Techniques, vol. 45, (1997) p. 898.
- 6) David M. Pozar, Microwave Engineering, 2nd ed., New York: John Wiley & Sons, Inc., 1998, chapter 4.
- 7) M. Topper, K. Scherpinski, R. Hahn, O. Ehrmann, H. Reichl, C. Schmaus, and F. Bechtold: Int. Synp. on Advanced Package Materials, (1998) p. 63.

- 8) J.S. Hong and M. J. Lancaster: Microstrip Filters for RF/Microwave Applications (Wiley, New York, 2001), Chap. 5, p. 121.
- 9) A. I. Zverev: Handbook of Filter Synthesis (Wiley, New York, 1967) Chap. 6, p. 290.
- 10) D. Budimir: Generalized Filter Design by Computer Optimization (Arectech House, Norwood, 1998) Chap. 4, p. 81.
- 11) C. Q. Scrantom and J. C. Lawson: IEEE MTT-S Sym. Tech. 193 (1999) p. 626.
- 12) D. J. Dubetsky, W. Falls, L. W. Herron, H. Junction, Raj N. Master and W. Fall: U.S. Patent 4340436 (1982).
- 13) F. P. Lautzenhiser, Edmar M. Amaya, W. Hochheimer, and J. Thomas: U.S. Patent 6743534 (2004).
- 14) Hammond, Mark Stuart, Tormey, Ellen Schwartz., Thaler, Barry Jay, Hozer, Leszek, Chen, Hung-tse Daniel, Geller, Bernard Dov, Frederickson and Gerard: U.S. Patent 6739047 (2004).

- 15) Ashok N. Prabhu, and Barry J. Thaler: U.S. Patent 5085720
(1996).
- 16) Kurt R. Mikeska, Wilmington, Daniel T. Schaefer, Newark,
Richard H. Jensen, and Wilmington: U.S. Patent 5581876 (1992).
- 17) Horn, Debra S., Minehan, Willian T., Volmering, James E. and
Weidner, Ken: Coors Electronic Package Company Chattanooga,
1994.
- 18) Jau-Ho Jean and Chia-Ruey Chang: J. Am. Ceram. Soc. 3084 (1997)
p. 80.
- 19) J. Y. Hsu, W. S. Ko, H. D. Shen, and C. J. Chen: IEEE Trans. Magn. ,
30, (1994) p. 4875.
- 20) S.F. Wang, Y.R. Wang, T.C.K. Yang, C.F. Chen and C.A. Lu:
Scripta. Mater., 43, (2000) p. 69.
- 21) S.F. Wang, Y.R. Wang, T.C.K. Yang, P.J. Wang, and C.A. Lu:
Journal of Magnetism and Magnetic Materials, 217, (2000)
p. 35.

- 22) E. Rezlescu, N. Rezlescu, C. Pasnicu, and M.L. Craus: J. Magnetism and Magnetic Materials, 157/158, (1996) p.487.
- 23) J.Y. Hsu, W.S. Ko and C.J. Chen : IEEE Trans. on Magnetism, 31[6], (1995) p. 3994.
- 24) K.G. Brooks and V.R.W. Amarakoon : J. Am. Ceram. Soc., 74[4], (1991) p. 851.
- 25) Y. Tamamoto, A. Makino, and T. Nikaidou : J. Phys. France Suppl. C17 (1997) p. 123.
- 26) J.Y. Hsu, W.S. Ko , H.D. Shen and C.J. Chen: IEEE Trans. on Magnetism, 30, (1994) p. 4875.
- 27) J.H. Jean and T.K. Gupta: J. Mater. Res. 7 (1992) p. 3103.
- 28) L.S. Chen, C.S. Hsi, S.L. Fu, and J.Y. Lin, : Jpn. J. Appl. Phys., 40, (2001) p. 123.
- 29) H.T. Kim and H.B. Im: IEEE Trans. Magn., 18, (1982) p. 1541.
- 30) G.C. Jain, B.K. Das, and N.C. Goel, J. Am. Ceram. Soc., 62, (1979) p. 79.

31) L.S. Chen, C.S. Hsi, S.L. Fu, and J.Y. Lin, : Jpn. J. Appl.
Phys., 39, (2000) p. 150.



Resume

我出生在一個幸福小康的鄉下家庭，父母已退休，從小對子女管教甚嚴，灌輸了很多正面的做人做事的觀念，使我面對任何事都能以樂觀積極的態度去面對。

我國小與國中都是在頭份完成，一直是田徑隊成員，讓我鍛鍊良好的體魄。國三時獨自北上參加北區高中聯招，考上板橋高中，雖一度為沒考上理想志願而傷心，但豐富的高中生活，很快地讓我忘記難過。我一進板橋高中即被選當班長、儀隊大隊長、合唱團副團長等幹部，忙碌中讓我學會如何安排時間及與人相處，也培養了我領導能力。因自高中獨自在台北求學，因此養成了相當的獨立性。

上大學(中原物理系)四年當中，我接受理論科學的訓練，除修習基礎課程外(光學、電磁學、量子物理、熱力學等)，也選修較有趣的應用課程(光電半導體元件導論、光學材料、半導體物理導論、光學設計、應用光學等)。由於個性隨和，在參加許多社團當中，結交許多朋友，並認知到團隊合作的重要與力量。此外我利用課餘時間兼職家教，這經驗讓我養成高於他人的抗壓性，也學習到如何的有效安排時間。

大四那年，我在行政院核能研究所跟著藍山明老師，先從事X光螢

光分析及碘化汞偵測器的研究，而在即將離開的半個月，也參與組裝生產藍光二極體的管型爐與測試。這段期間讓我的知識成長很多，而我也開始對應用材料產生興趣。

進入成功大學資源工程所(原礦冶暨材料工程研究所)礦物材料組，一方面進行碩士論文的研究，一方面也擔任掃描式電子顯微鏡(SEM)的操作助教，並協助成立熱分析實驗室，完成熱分析儀(DTA)及熱膨脹儀的組裝與測試。而在課堂上，我選修了結晶化學、相平衡、結晶物理學、高等燒結理論及電子顯微鏡，X光分析的課，讓我對材料從前段製作到後段的性質測試，有完整且一系列的觀念及經驗。

工研院材料所是我離開學校後的第一份工作，主要從事玻璃陶瓷材料及藉由陶瓷中添加玻璃以降低燒結溫度之研究。在這三年半的期間，除了在學術研究或邏輯分析上有所突破外，同時也享受將所學充份應用於工業上之成就感，也讓我對繼續攻讀博士更多了一份堅持。之後幸運的考上交大材料所，接受林鵬教授的指導攻讀博士學位，研究的領域為低溫共燒玻璃陶瓷材料，這當中還獲得了二個玻璃陶瓷材料的中華民國發明專利。目前在日商住友集團下的住華科技單任研發主管職務，從事開發偏光板的研究工作，希望在畢業後能有機會擔任教職，將所學貢獻給社會。

Publication list

1. 饒瑞珠, 劉元文, 黃啟原, 顏富士 “氧化鋯含量對陳化的 ZTA 膠體粉末之燒結行為影響”, 中國礦冶工程學會 1995 年度年會, 1995 年 11 月 26 日.
2. 饒瑞珠, 黃啟原, 顏富士 “氧化鋁/氧化鋯共沉粉末的相生成與燒結行為”, 中華民國陶業研究學會 1995 年度年會, 1995 年 4 月 23 日.
3. 饒瑞珠, “氧化鋁/氧化鋯共沉粉末的相生成”, 國立成功大學資源工程研究所, 碩士論文, 1995.
4. 劉元文, 饒瑞珠, 顏富士, 黃啟原 “共沉氧化鋁微粉的相生成”, 中國材料科學學會 1996 年度年會論文集第一冊, 論文編號 S4A-4, 348-351 頁, 1996 年 10 月 3 日至 4 日.
5. 饒瑞珠, “與杜邦生胚匹配之金屬膏配方開發”, 工業技術研究院工業材料研究所技術報告, (1997).
6. 饒瑞珠, 謝彩綿 “大孔徑擠壓填孔技術開發”, 工業技術研究院工業材料研究所技術報告, (1997).
7. 饒瑞珠, “生胚通孔技術及疊壓製程”, 第一屆國際多層低溫共燒陶瓷技術研討會, (1998).
8. 饒瑞珠, “以實驗計劃法提高印刷式填孔的良率”, 工業材料, 144 頁, 143 期, (1998).
9. 饒瑞珠, 曾英蘭 “以實驗計劃法提高網版印刷品質”, 工業材料, 136 頁, 136 期, (1998).
10. 饒瑞珠, “高精密度多層陶瓷元件”, 中華民國專利發明第 197763 號(專利期間: 民國九十三年二月十一日至民國一十二年一月二十七日)
11. 李文熙, 蘇哲儀, 李俊德, 饒瑞珠, “抑制低溫陶瓷燒結收縮之方法及抑制層”, 中華民國專利發明第 202000 號 (專利期間: 民國九十三年五月十一日至民國一十一年三月六日)
12. J.C. Jao, and Pang Lin, ” Method of Estimating Dielectric Properties of Dielectric Layers in Low-Temperature-Cofired Ceramic Devices” Jpn. J. Appl. Phys., Vol. 45 (2006) No. 11, pp. 8751-8754.

13. J.C. Jao, and Pang Lin, " Self-Constraining Method for Low Shrinkage of Low-Temperature-Cofired Ceramic Devices" Jpn. J. Appl. Phys. Vol. 46 (2007) No. 6A, pp. 3654-3657.
14. J.C. Jao, Pang Lin, and Sea-Fue Wang, " Characterization of Inductor with Ni-Zn-Cu Ferrite Embedded in B_2O_3 - SiO_2 Glass" Jpn. J. Appl. Phys. Vol. 46 (2007) No. 9A.

